Journal of Hydrology 674 (2026) 135498

Contents lists available at ScienceDirect

Journal of Hydrology

journal homepage: www.elsevier.com/locate/jhydrol

Research papers

A Bayesian segmentation method for reservoir spread area extraction using synthetic aperture radar and water occurrence

Lei Xie [a], Wenbin Xu [a,*], Kun Jiang [a], Lei Zhao [a], Eslam Ali [b]

[a] School of Geosciences and Info-physics, Central South University, China
[b] Public Works Department, Faculty of Engineering, Cairo University, Egypt

ARTICLE INFO

This manuscript was handled by Ashok Mishra, Editor-in-Chief, with the assistance of Xinyi Shen, Associate Editor

Keywords:
Reservoir water spread
Bayesian segmentation
SAR
Water occurrence
Sentinel-1
Himalayan foothills

ABSTRACT

Accurate mapping of reservoir spread areas is essential for watershed management and sustainability. Synthetic Aperture Radar (SAR) provides cloud-penetrating capability, and enabling a better and more stable temporal resolution than optical systems. Nevertheless, existing SAR-based water extraction algorithms face critical limitations from time-varying backscatter modulations, e.g., wind, vegetation, soil moisture, topography. Here, we propose a new Bayesian segmentation method combining SAR and water occurrence data to explore reservoir dynamics under different weather conditions. Several false alarm cases, such as mountain shadows, breezes, moist soil, vegetation were corrected using probabilistic integration of complementary SAR and water occurrence. The proposed method was applied and validated at four large reservoirs in Lesser Himalayan foothills using more than 1000 acquisitions of Sentinel-1 data, optical imagery, *in situ* measurements, and comparisons of existing methods. The results showed a 3–10% improvement in segmentation accuracy and a 6–18% increased temporal density and uniform snapshots of inundation changes. We suggest that this weekly mapping of reservoir dynamics is complementary to *in situ* gauges for multiple applications, especially in areas with persistent clouds, such as the Amazon and Southeast Asia.

1. Introduction

Over the past seven decades, reservoir numbers have surged from ~ 5000 to ~ 60,000 (Hjorth and Bengtsson, 2012). This has profoundly reshaped terrestrial water storage, creating a total capacity of 7000–10,000 km^3, which corresponds to 17% of global river runoff (Boulange et al., 2021; Dong et al., 2022; Revilla-Romero et al., 2016). Reservoirs are highly dynamic systems in which inter-annual and seasonal variations are controlled by both human manipulation and climate (Ahmad et al., 2014). Therefore, accurate mapping and detailed knowledge of reservoir water-spread areas are critical for research and practical application of water resource allocation, ecosystem and climate change, and geological hazard mitigation (Shen and Zhang, 2016; Wheeler et al., 2020; Xie et al., 2022; Zhao et al., 2022).

Although inland water body mapping is a well-established application in the remote sensing community, the trade-off between spatio-temporal resolution and cloud coverage impedes the retrieval of dense and fine reservoir dynamics (Klein et al., 2017; Zhang et al., 2017a). Interpolation methods based on auxiliary data (e.g., topography) and sequence inference (e.g., moving windows) are pathways that improve temporal resolution. To further reduce the uncertainty in sequence interpolation/inference, medium-to-coarse optical data (e.g., MODIS at 250 m) with daily global coverage are widely used (Klein et al., 2017, 2021). However, their relatively coarse spatial resolution of hundreds of meters limits application in small reservoirs and catchments. Another option is to achieve a finer resolution and free-archived missions (e.g., Landsat series and Sentinel-2). Many products based on decision-tree and thresholding methods can retrieve inland water bodies at 20–90 m resolution (Pekel et al., 2016; Yamazaki et al., 2015), fulfilling the requirements of inland water mapping tasks (e.g., terrestrial water budget analysis). Nevertheless, the degradation of temporal resolution in the raw data handicaps inter-month monitoring because most reservoirs are situated in cloudy areas (Zhang et al., 2017b). Furthermore, the temporal distribution of cloud-free images is unequal and controlled by the regional climate. Even using composites from the 5-day revisiting Sentinel-2 satellite (Yang et al., 2020), > 30 years of Landsat collection (Pekel et al., 2016), or the daily PlanetScope satellites (Valman et al., 2024), capturing cloud-free images to monitor weekly time series is difficult (Donchyts et al., 2022), resulting in areas of “no data” in the vicinity of reservoirs.

* Corresponding author.
E-mail address: wenbin.xu@csu.edu.cn (W. Xu).

https://doi.org/10.1016/j.jhydrol.2026.135498
Received 22 June 2023; Received in revised form 30 January 2026; Accepted 10 April 2026
Available online 12 April 2026

To overcome the unfavorable atmospheric conditions affecting optical sensors, weather-independent synthetic aperture radar (SAR) data provides an effective tool for the extraction of floods (Panahi et al., 2022), lakes (Dai et al., 2021), ponds (Perin et al., 2021), river (Yu et al., 2022), and reservoirs (Vanthof and Kelly, 2019). Threshold-based methods are popular in SAR water-extent detection (e.g., Dai et al., 2021; Vanthof and Kelly, 2019) because of the distinct features of specular reflectance on an open-water surface. Because amplitudes are manifestations of different factors, various factors in the reservoir area can affect the backscattering property (e.g., soil moisture, wind, turbidity, and shadow) (Fig. 1) and result in false-alarm detection. Therefore, local thresholding methods that use land-type as a prior information (Liang and Liu, 2020) or adaptative image block separation (Tan et al., 2023) can achieve more accurate segmentation of bimodal distributions. However, these approaches suffer from the potential intersection errors when outputs of multiple-polarizations are involved. Learning-based methods transferred from optical images, such as convolutional neural network (CNN)-based methods, often require SAR benchmarks for model training and are challenged by the low-texture information of the microwave spectrum (Shang et al., 2022) and complex imaging conditions (Zhang et al., 2021). To address these challenges, efforts have paid to enhance the training datasets. For example, the imbalance of labeling categories can be mitigated by introducing a weighted focal loss function, which decreases invalid training caused by the large number of background labels (Zhang et al., 2021). Another enhancement involves expanding the volume of training samples by generative adversarial network (GAN), such as pairing unlabeled SAR images with the optical images via a cycle-consistent GAN (Li et al., 2021; Saha et al., 2021). Modern transformer-based architecture combine the CNN and the transformer encoder to create the semantic relationship between the optical and SAR segmentations (Dong et al., 2023), which obtains sharper and higher-resolution of water boundaries using Sentinel-1. Statistics-based methods using contextual information demonstrate the capability of SAR water segmentation, but unsupervised segmentation typically rules out specific backscattering features (D'Addabbo et al., 2016; Fjortoft et al., 2003; Goumehei et al., 2019). For example, a conditional probability density function with seasonal backscattering variations is introduced in mapping the flooding water extension. It considers the temporal change of flooding inundation, but does not consider the roughness and soil moisture change in the reservoir area (Schlaffer et al., 2017). The Wishart distribution with Markov Random Field (WMRF) can formulate the water and lands with different back-scattering properties in semi-arid reservoirs. But it may fail to correctly recognized bare soil due to the similar low back-scattering feature (Goumehei et al., 2019). Similar empirical model using statistical features measured by gamma functions are adopted to the large-scale lake segmentation, but a distance-based correction is used to suppress the false alarms from the land (Zhou et al., 2020). Therefore, segmentation may be contaminated by similar lakeshore targets, and additional post-processing steps, such as morphological operations, clustering, and manual correction, are unavoidable to maintain the spatial continuity. To further improve the near-lakeshore segmentation, a Kolmogorov-Smirnov hypothesis test is applied based on the probability of false alarm, but the different polarization bands cannot be involved simultaneously (Ferrentino et al., 2020). To sum up, the primary and recurring problems in the existing SAR-based methods for reservoir water extraction lie in: 1) misclassification arises from overlapping backscatter distributions such as wind-roughened surface Bragg scattering, riparian soil moisture dynamics, and topographic shadowing; 2) fragmented boundaries due to the noise and artifacts which require adaptive post-processing such as filtering and morphological operations; 3) The training pipeline encounters inherent limitations due to the scarcity of high-fidelity SAR-derived annotations specific to reservoir environments.

To solve the existing limitations, this study proposes a Bayesian optimization method based on a hidden Markov random field (HMRF) for reservoir water-spread area segmentation. In contrast to existing methods, the proposed method can integrate polarization information (either single- or dual-polarization) and water occurrence, and can be applied easily because of the accessibility of these two types of inputs. It also does not need any training samples and post-processing steps to delineate reservoir boundary through an iterative probability way of

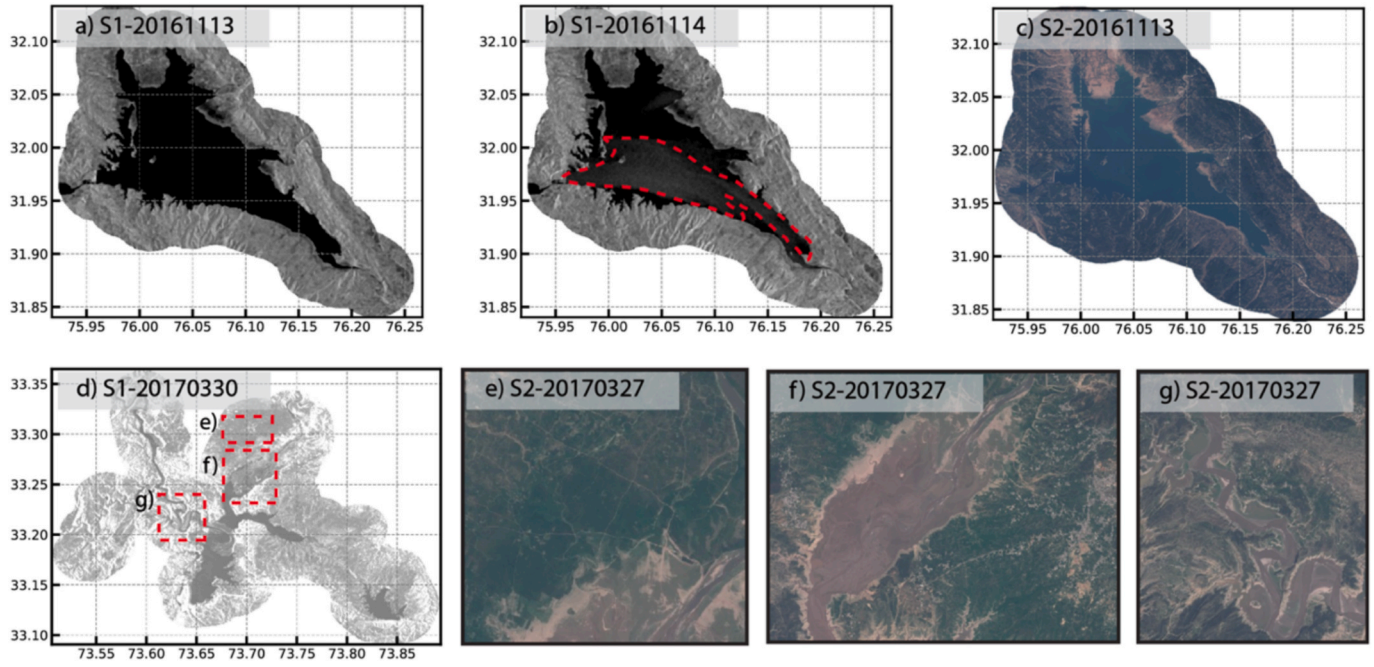

Fig. 1. Examples of wind-induced Bragg scattering and moist soil near the shoreline: (a) the calm water surface without Bragg scattering in S1 image; (b) the windy water surface with Bragg scattering outlined by the red polygon in S1 image; (c) the comparison from S2 image; (d) the moister soil near the shoreline in S1 image; (e-g) the enlarged view of comparisons from S2 image. S1: Sentinel-1, S2: Sentinel-2. (For interpretation of the references to colour in this figure legend, the reader is referred to the web version of this article.)

estimation. We validated the proposed method in four reservoirs with different hydrological and back scattering features in the Himalayan foothills using Sentinel-1 (S1) data from 2015 to 2021. The results showed good performance and were validated by two independent measurements and existing methods. We also demonstrated the proposed method can increase success rate for the reservoir mapping, supporting a finer temporal resolution of one week.

2. Method

The proposed method aims to enhance the feature presentation of the gray-level band and correct the false-alarm segmentation owing to water variations near the shoreline. The workflow of the method contains three modules (Fig. 2): 1) SAR data preprocessing; 2) Band combination; 3) Bayesian segmentation. To validate the accuracy of proposed method, we manually delineated optical images (i.e., Landsat-8 and Sentinel-2) with the same acquisition dates as the SAR data, and collected gauge data from Central Water Commission (CWC) of India. (See section 3 and Table S1 for a detailed data description and Section 4.3 for a detailed comparison).

2.1. SAR preprocessing

We first collected S1 Ground Range Detected (GRD) data according to boundaries from the Global Reservoir and Dam (GRanD) database (Lehner et al., 2011). Segmented frames for the target reservoirs were stitched to increase the number of available observations. We buffered the region of interest by reservoir size to cover seasonal variations and reduce the computational burden. We selected the polarizations as vertical transmit-vertical receive (VV) and vertical transmit-horizontal receive (VH) as it is the most common imaging mode in the modern SAR mission such as Sentinel-1 and RadarSat-2. All available GRD scenes were processed following standard steps and converted to decibels (*dB*), i.e., the sigma naught (σ^0), using logarithmic scaling; these steps were restituted orbit correction, border and thermal noise removal, radiometric calibration, and topography correction. We applied a refined Lee sigma filter with a 3 × 3 window to suppress the speckle noise (Lee et al., 2009).

2.2. Input band combination

We paired the SAR data with water occurrence data from the European Commission–Joint Research Centre (JRC). We adopted both JRC monthly frequency data and historical frequency data (i.e., the probability of water occurrence), which count the surface water occurrence by Landsat data from March 1984 to December 2021. Each S1 image was resampled into a grid size of 30 × 30 m to match the monthly frequency data or historical frequency data (used when monthly data were unavailable mainly due to the dense cloud coverage, e.g., the January and December in the Pong reservoir).

Therefore, given $Y = \{y_1, \ldots, y_N\}_{2\times N \vee 3\times N}$ is the observation set for N pixels at a specific location y_i, the input has four possible combinations based on the SAR and water occurrence data:

$$y_i = \begin{cases} \{VV_i, VH_i, WM_i\}, \ dual-polar\ and\ monthly\ water\ occurence \\ \{VV_i, VH_i, WH_i\}, \ dual-polar\ and\ historical\ water\ occurence \\ \{VV_i, WM_i\}, \ single-polar\ and\ monthly\ water\ occurence \\ \{VV_i, WH_i\}, \ single-polar\ and\ historical\ water\ occurence \end{cases} \quad (1)$$

where *VV*, *VH*, *WM*, and *WH* refer to the *VV* and *VH* polarization modes, and the monthly and historical water occurrence data (e.g., JRC), respectively.

2.3. Bayesian segmentation

We propose the application of the Bayesian estimator of the HMRF to integrate SAR and water occurrence data, as these two types of

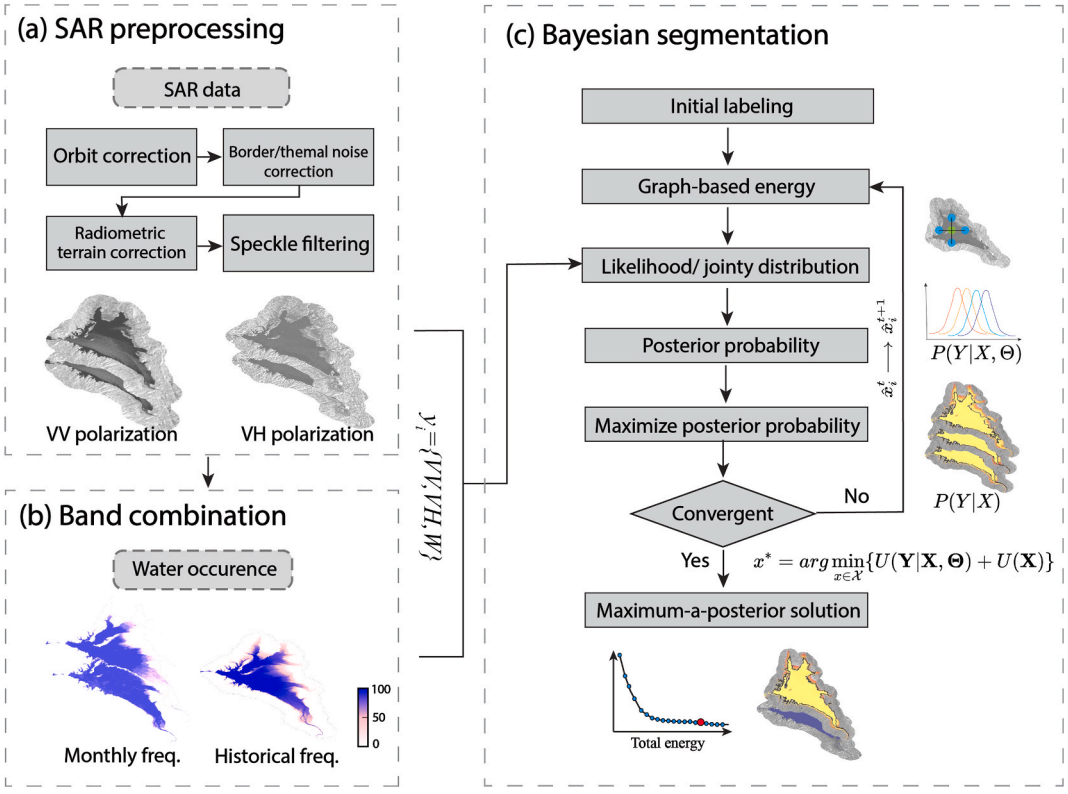

Fig. 2. The schematic workflow for the proposed method: (a) SAR preprocessing; (b) Input band combinations for SAR and water occurrence data; (c) Iteration procedure for the Bayesian segmentation.

observations are independent and statistically similar to follow the multivariate Gaussian distribution. The HMRF model considers statistical characteristics in both the features (i.e., backscattering) and physical space (i.e., spatial correlation) (Zhang et al., 2001).

Different from the existing probabilistic-based SAR backscatter statistics method (Goumehei et al., 2019; Schlaffer et al., 2017), the observation matrix $Y = \{y_1, ..., y_N\}_{2\times N \vee 3\times N}$ contains both SAR and water occurrence as represented by Eq. (1). $X = \{x_1, ..., x_N\}_{1\times N}$ is the set of labeled images, that is, the segmentation configuration (e.g., Fig. 3). Using the maximum *a posteriori* probability (MAP) criterion under Bayesian theory for the unsupervised classification, a target solution $\hat{x}$, i.e., an estimate of the true label x^*, is used to find the optimization as

$$\hat{x} = \underset{x\in X}{argmax}\{P(Y|X,\Theta)P(X)\} \tag{2}$$

where $\Theta = \{\theta_i \in L\}$ is the iterative parameter set of the segmentation. While the proposed method is unsupervised, for our binary segmentation task of land and water, we predefined the semantic labeling set as $L = \{L_{land}, L_{water}\} = \{0, 1\}$.

According to the Hammersley–Clifford theorem, the prior probability $P(X)$ is subject to the Gibbs distribution (Geman and Geman, 1984), and can be derived as

$$P(X) = \frac{1}{Z} exp(-U(X)) \tag{3}$$

where Z is a normalized constant equal to the summation of multiplication of the energy function $U(X)$, and $U(X) = \sum_{c\in C} V_c(X)$ is determined by potential $V_c(X)$ with a given clique c in a four-connected neighbouring pixel system. For the conditional independent pair (x_i, y_i), the likelihood distribution $P(Y|X,\Theta)$ can leverage both SAR backscattering observations and water occurrence priors, as

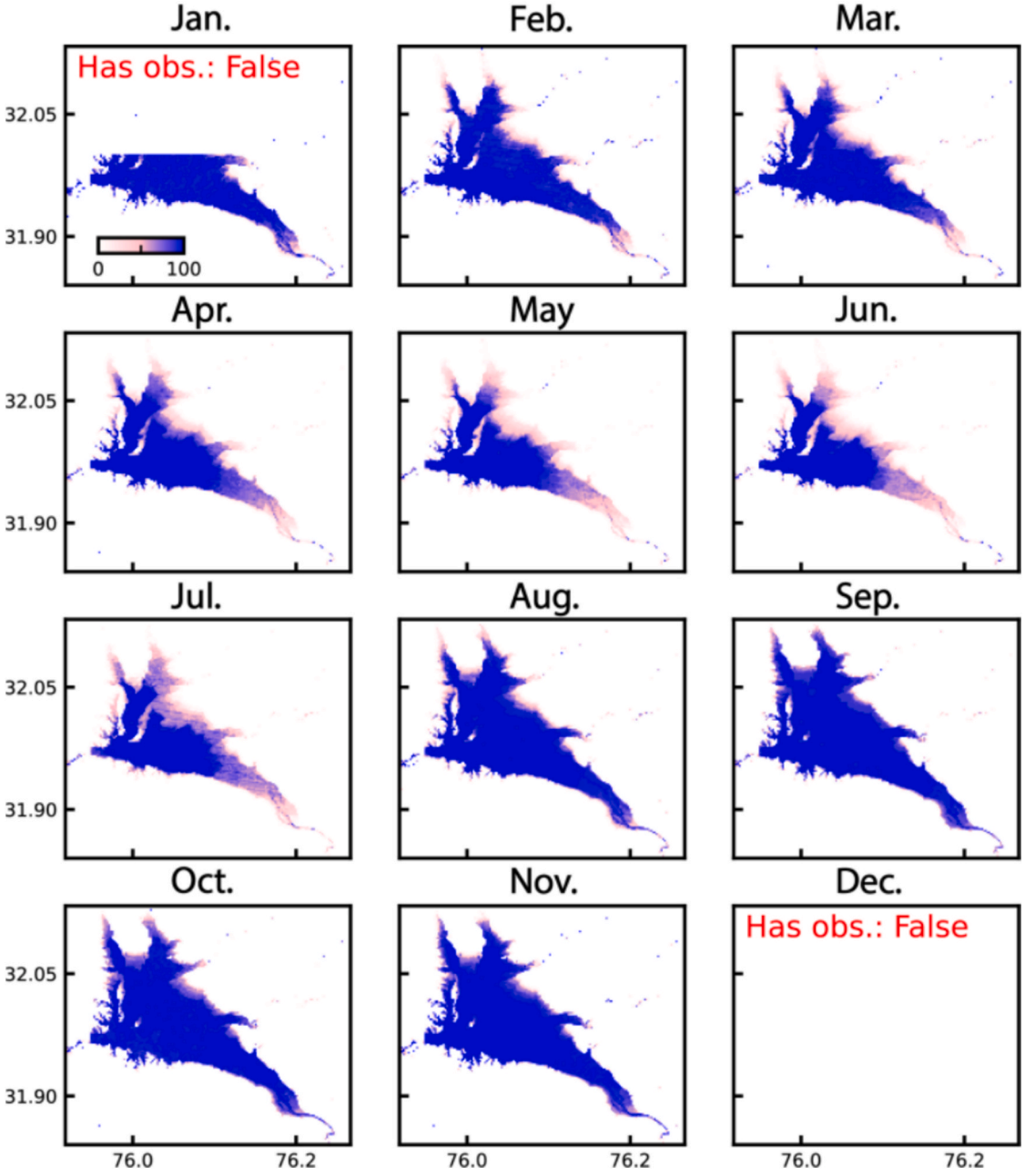

Fig. 3. Example of JRC monthly frequency data on the Pong reservoir. It shows a data vacancy in January and December, and the monthly data will be substituted by historical data for the inputs as shown in Eq. (1).

$$P(Y|X) = \prod_{i=1}^{N} P(y_i|x_i) \tag{4}$$

Accordingly, the MAP estimation in (2) can be represented by energy minimization as

$$x^* = \underset{x \in X}{argmin}\{U(Y|X,\Theta) + U(X)\} \tag{5}$$

where the likelihood energy $U(Y|X,\Theta)$ to quantify the optimal water-land classification is

$$\begin{aligned} U(Y|X,\Theta) &= \sum\nolimits_i U(y_i|x_i,\theta_i) \\ &= \sum\nolimits_i \left[\frac{(y_i - \mu_{x_i})^2}{2\sigma_{x_i}^2} + log(\sigma_{x_i}) \right] \end{aligned} \tag{6}$$

in which μ and σ are the mean and standard deviation for the labeled pixels, respectively. Here, we use the expectation−maximization (EM) method to iteratively estimate the parameter set Θ (Zhang et al., 2001), i.e., the maximization of the total posterior distribution. To obtain a good initial inference, we first allocate the initial labels and estimate the initial parameter set Θ^0 according to the GRanD, i.e., the mean and standard deviation for the in-polygon pixels. The E-step for the condition expectation $E(\bullet)$ at the t-th iteration is

$$\begin{aligned} E(\Theta|\Theta^t) &= E[logP(X,Y|\Theta)|Y,\Theta^t] \\ &= \sum\nolimits_{x \in X} P(X|Y,\Theta^t) logP(X,Y|\Theta) \end{aligned} \tag{7}$$

We maximize the conditional expectation $E(\Theta|\Theta^t)$ to obtain the next iteration of the parameter estimate set Θ^{t+1} in the M−step. The labeling configuration is updated $\hat{x}_i^t \longrightarrow \hat{x}_i^{t+1}$ until convergence of the energy function (5) or predefined iteration number is achieved. Once the MAP or expected solution is reached (e.g., the energy descent is less than 1% for each iteration), the posterior distribution labels for all given pixels are updated to obtain the optimized inundated segmentation.

2.4. Iterative process

In the proposed method, the numbers of iteration need to be determined to achieve a convergent solution, while balancing the trade-off between the computation burden and optimization performance. Using the total energy as an indicator (e.g., Fig. 4), we terminate the iteration when the descent gradient ΔT less than 1% from the last round of iteration,

$$\Delta T = \left[U\left(Y^{t+1}|X^{t+1},\Theta^t\right) + U\left(X^{t+1}\right)\right] - \left[U(Y^t|X^t,\Theta^t) + U(X^t)\right] \tag{8}$$

in which t indicates the *i-th* iteration, and other notations are the same as in Eq. (5). In practice, we set up the 20 iterations for the burn-in period to remove the initial unstable solution and feature the model parameters. We examine all 1430 observations, and 1407 (98.4%) images converged in fewer than 100 iterations. The remaining 23 observations (1.6%) met the threshold for energy gradient descent within 200 iterations. In addition, comparing with the manually delineate boundaries, the estimated total energy $U(Y|X,\Theta)+U(X)$ also indicates the achievement of convergence with an average difference of 1.3%.

This iterative segmentation process explicitly addresses the unfavorable conditions under which the ideal bimodal backscattering distribution between water and land does not hold. First, wind-roughened Bragg scattering primarily affects the co-polarized band and leads to severe overlap between water and land backscattering distributions. For example, the VV band exhibits two dominant peaks at approximately −10.0 dB and −14.9 dB (Fig. 5a), where wind-enhanced backscattering shifts part of the water pixels toward higher amplitudes, weakening the separability of the water peak. In contrast, the VH band remains less sensitive to wind-induced surface roughness and shows a stable and dominant peak around −26.1 dB corresponding to open water (Fig. 5c and d). By iteratively fusing dual-polarization information over 100 iterations, the VV-band water peak converges from the wind-contaminated −10 dB toward −15.7 dB (Fig. 5b), while the segmentation in VH-band peak remains stable at −26.1 dB. This convergence effectively suppresses wind-related misclassification raised from the VV band.

Second, soil-moisture variability along lakeshore introduces an additional backscattering mode that violates the ideal bimodal assumption. In the VH band, moist soils near the lakeshore and river outflow produce reduced backscattering, forming a third peak near −23.2 dB (Fig. 5c), which partially overlaps with the water distribution. To explicitly characterize this effect, we incorporated the Normalized Multi-band Drought Index (NMDI) (Wang and Qu, 2007), which provides enhanced sensitivity to soil moisture variations compared with SAR observations. The NMDI distributions (Fig. 5g and h) indicate elevated moisture levels (0.58–0.65) along the lakeshore (Area h1) and the outflow river corridor (Area h2). These areas are subsequently excluded during iterative refinement because they exhibit low water-occurrence probability and consistently high backscattering in the VV band.

Third, speckle noise and SAR-specific artifacts typically require ad-hoc filtering or morphological post-processing, which can fragment water boundaries. In this study, such post-processing is largely avoided by incorporating long-term water occurrence probability, as the spatial smoothness prior, derived from the JRC dataset. As shown in Fig. 5e and f, pixels with low water-occurrence probability (<95%) are sparsely and uniformly distributed, enabling the iterative segmentation to naturally suppress noise-induced false positives by the MRF spatial regularization without introducing artificial boundary smoothing.

Overall, the proposed iterative segmentation framework resolves wind-induced backscatter overlaps, soil-moisture-related ambiguity, and speckle-driven fragmentation through physically informed multi-source constraints rather than empirical thresholding or heavy post-processing.

3. Study area and datasets

In this study, we used four reservoirs located in the Lesser Himalayan foothills (Fig. 6) with different hydrological and topographical features and complex SAR backscattering properties due to the significant seasonal water variability for the demonstration, from west to east, they are: (1) Mangla Reservoir lies between 33.22° N and 73.68° E in Pakistan. It was created by one of world's largest embankment dams, built up in 1965. It across the Jhelum River and Poonch River that affect both north Pakistan and Indus Basin (Adams and Ahmed, 1969). Intermittently cultivated areas along reservoir shorelines during low-water seasons exhibit variable soil moisture content, leading to the reduced SAR backscattering and subsequent false positive water detection. (2) Ranjit Sagar Reservoir situated in 32.46° N and 75.74° E in India. It built up in 2001, and greatly contributes to the irrigation and hydroelectricity for the Ravi River (Thakur et al., 2021). The dynamic water surface area (40–80 km^2) exposes mixed sediments and shoreline vegetation through frequent water level fluctuations, introducing spectral complexity in SAR imagery segmentation. (3) Pong Reservoir located at 32.00° N and 76.04° E on the Beas River in India. It was constructed in 1974 and also serves for the irrigation and hydropower needs (Adeloye et al., 2016). In this reservoir, wind-induced Bragg scattering during winter months significantly alters SAR backscatter patterns from calm water surface. (4) Bhakra Reservoir at 31.42° N and 76.46° E on Sutlej River, India. It was built up in 1963 and serves as one of the highest gravity dams in the world (Dau and Adeloye, 2021). Steep topographic gradients (slope degree of 26–39° near the lakeshore) generate geometric shadows that impede accurate water body delineation. Despite the features in SAR backscattering, the hydrological properties of these four reservoir are also closely related to the Indus River system and Himalayan fault system (Gupta and Rajendran, 1986; Mukhopadhyay and Khan, 2014; Xie

et al., 2021a). They are fed by major tributaries of the Indus River, and in-between the Himalayan mountainous area and lower Indus Basin. The river discharge is controlled by rainfall and snowmelt, and 50–80% of annual rainfall is received during the Indian summer monsoon (June to September) (Bookhagen and Burbank, 2010). Therefore, the minimum and maximum capacities of these reservoirs are at the onset of the snow-melting season (e.g., March–April) and end of the monsoon season (e.g., September–October), respectively. However, the intra-month variations of water-spread area, especially during the monsoon season, remain unclear owing to dense clouds.

To better evaluate the natural (e.g., vegetations, soil moisture) and anthropogenic variabilities (e.g., reservoir operations) in different

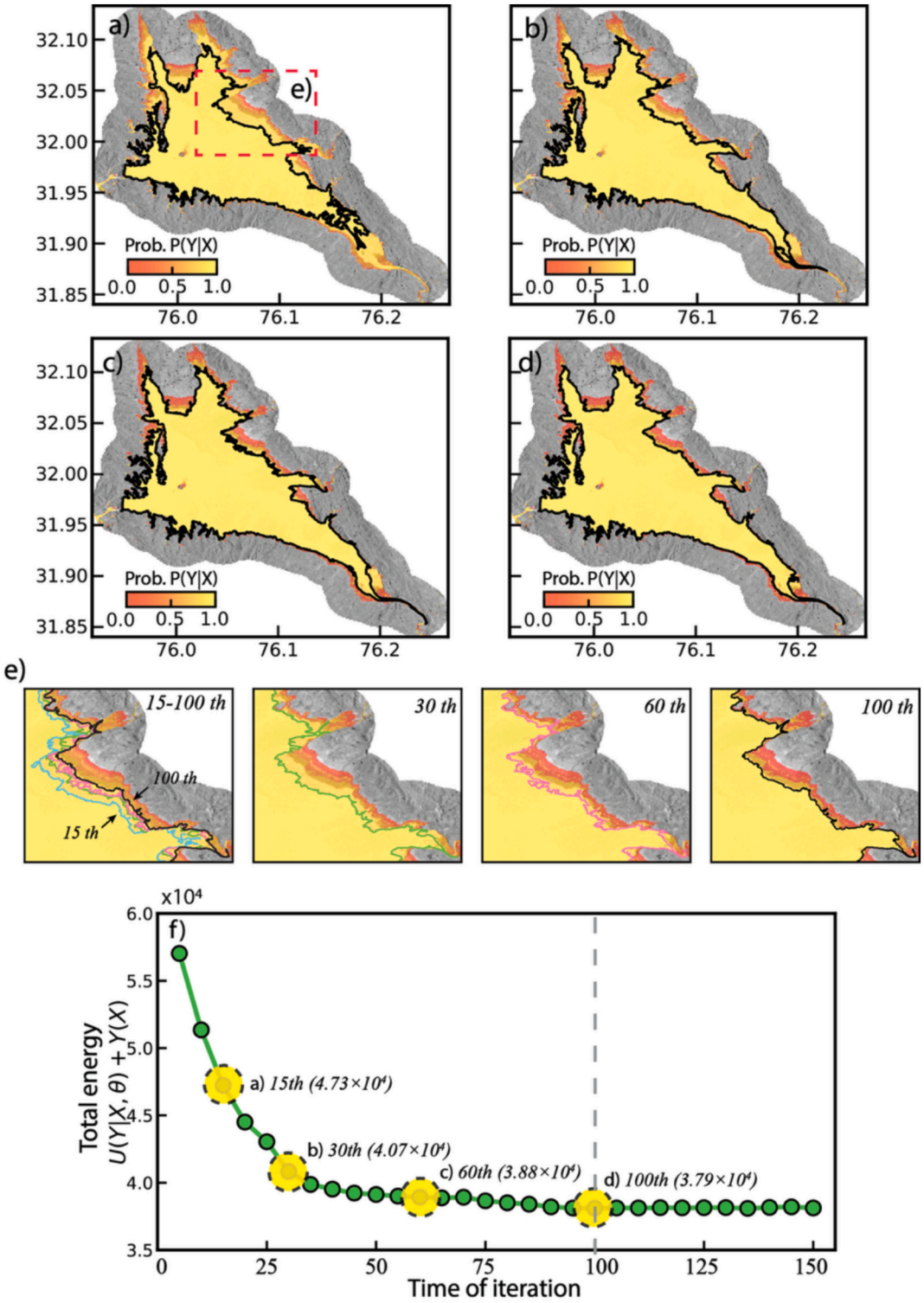

Fig. 4. The process of iteration for water segmentation. (a-d) The examples of posterior probability estimates $P(Y|X)$, the dashed red box indicates the geographical region of enlarged view; (e) the enlarged view of posterior probability estimates; (f) The changes of total energy during the 1-150th iterations (the green dots indicate every five steps); The total energy for the exemplified manual delineation boundary is 3.75×10^4. (For interpretation of the references to colour in this figure legend, the reader is referred to the web version of this article.)

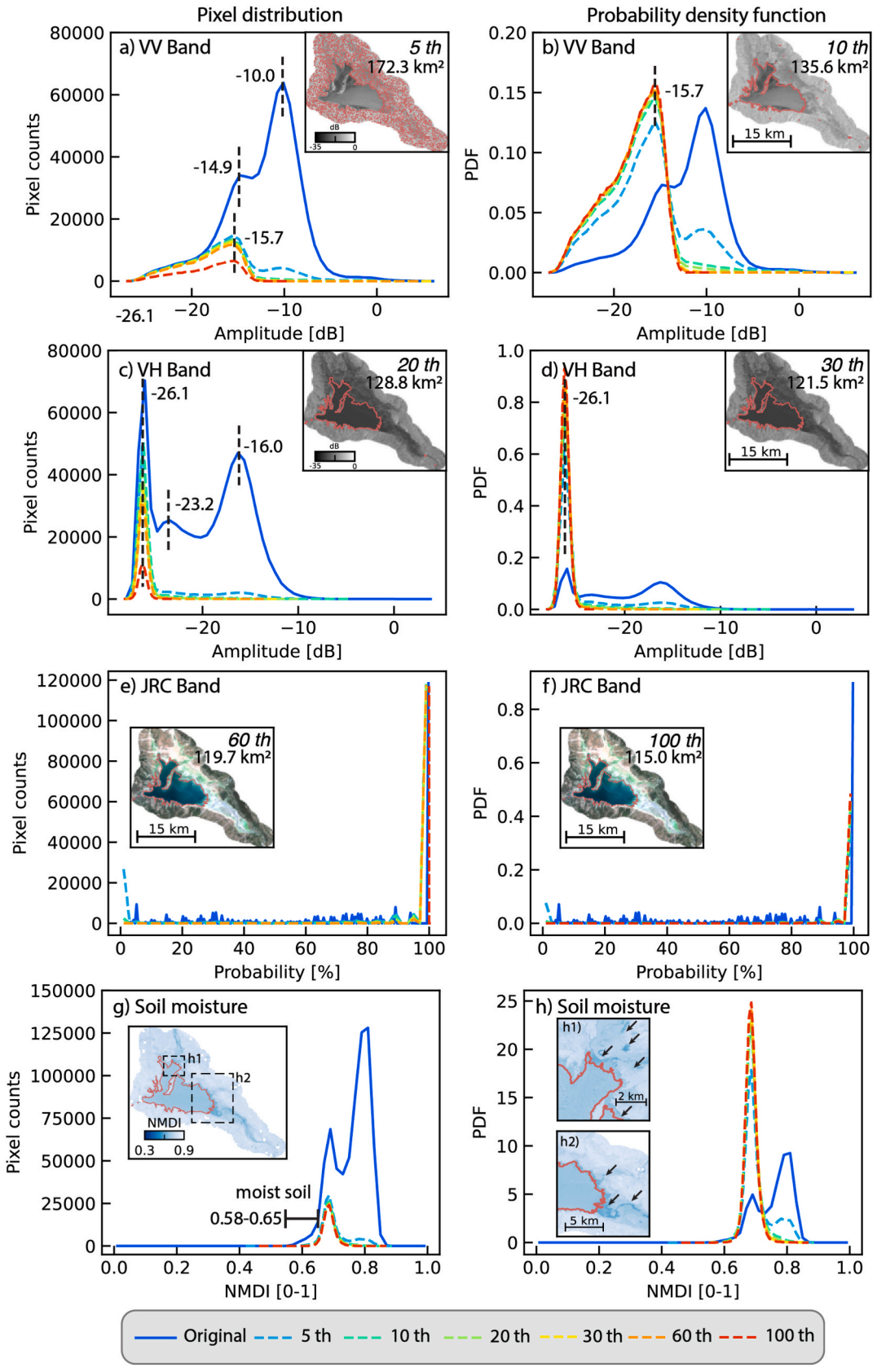

Fig. 5. Distributions of the iterative water segmentation process. (a–b) VV band; (c–d) VH band; (e–f) JRC; (g–h) NMDI. The solid blue curves represent the distributions of the original data, while the colored dashed curves indicate the pixels identified as water at different iteration steps. The black arrows indicate areas of moist soil. (For interpretation of the references to colour in this figure legend, the reader is referred to the web version of this article.)

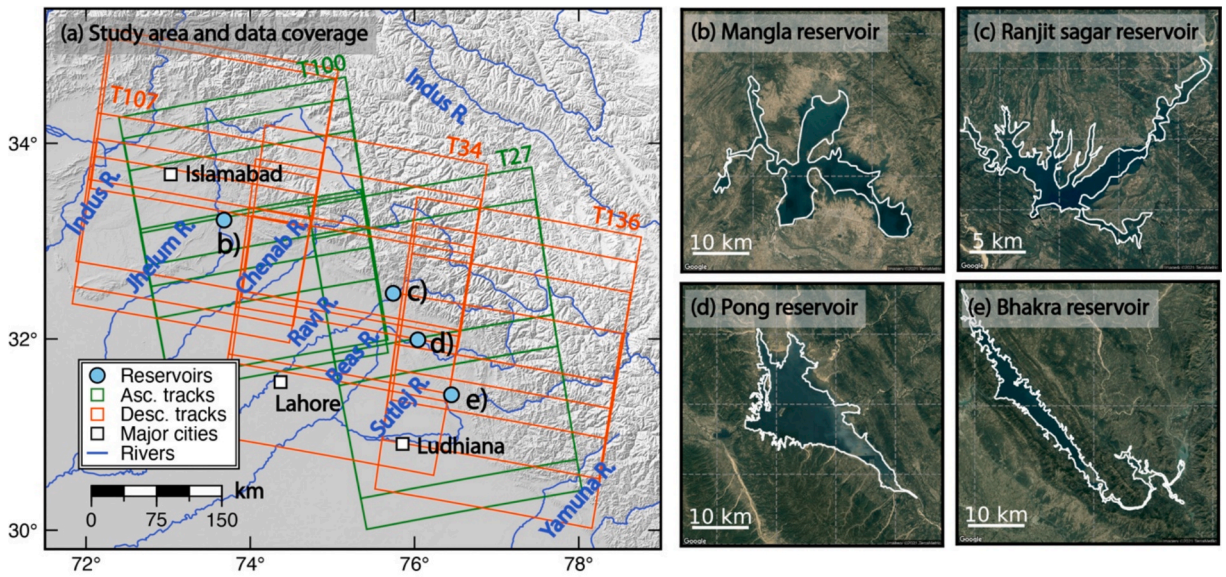

Fig. 6. Study area and data coverage. (a) Target reservoirs and Sentinel-1 footprints. The ascending and descending tracks are depicted in green and red rectangles, respectively. (b–e) Enlarged views of the selected reservoirs. (For interpretation of the references to colour in this figure legend, the reader is referred to the web version of this article.)

seasons, we select all available Sentinel-1 images in five tracks during 2015–2021 in the study area. From west to east, the selected reservoirs had 306, 334, 465, and 325 valid observations, respectively, after excluding contaminated scenes with radio frequency interference (please note that several scenes cover multiple reservoirs, see Table S1 for the detail acquisition date). In the early stage of the S1 mission

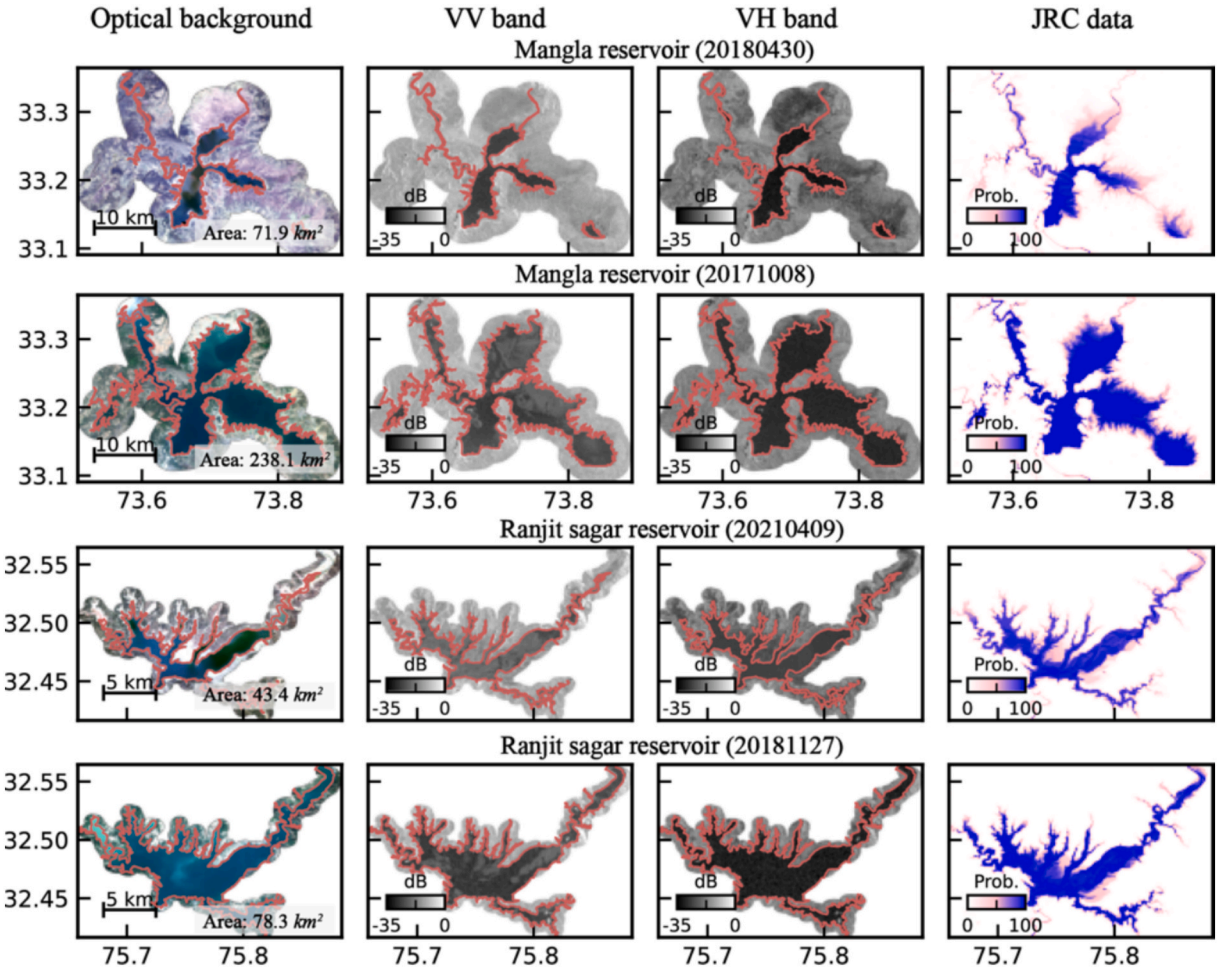

Fig. 7. The results of extracted water areas at low-water and high-water seasons in Mangla reservoir and Ranjit Sagar reservoir.

(2015), S1A only provided single-polarization data (VV) with a revisit period of 12–24 days. Starting in late 2016, most reservoirs were imaged by at least two tracks in dual-polarization mode (VV and VH) over 12 days by both S1A and S1B. In the Pong Reservoir, three overlapping orbital paths (i.e., T27, T34, and T136) improved the temporal resolution to better than six days.

To validate our method, in the Mangla Reservoir, we manually delineated the water area using optical imagery acquired on the same date as the S1 collection. Forty-five images from Sentinel-2 and Landsat-8 were selected for the quantitative evaluation (Table S1). For Ranjit Sagar, Pong and Bhakra Reservoirs, we collected the *in situ* gauge measurement from Central Water Commission of India, to conduct a cross-validation between water spread area and water level.

4. Results and discussion

4.1. Extracted water areas

The proposed method was validated across four hydrologically diverse reservoirs exhibiting distinct scattering regimes (Figs. 7 and 8). At Mangla reservoir's seasonal drawdown phase (33.31° N, 73.69° E; Fig. 7), transitional agro-floodplain zone exhibits polarization-dependent attenuation: VV (−16.1 ± 1.7 dB) to VH (−26.3 ± 2.2 dB), contrasting with permanent water bodies (−28.1 ± 1.5 dB in average). The proposed method fused the multi-feature of VV, VH, and JRC, achieving 71.9 km^2 water mapping, effectively decoupling soil moisture variations from different sensitivities of soil moisture to polarizations (Panahi et al., 2022). Second, at Ranjit Sagar reservoir, the proposed method can capture dynamic water surface area fluctuations (e.g., 43.4–78.3 km^2 in Fig. 7), under the condition of heterogeneously distributed Bragg scattering area on water surface with changing turbidity (Inserra et al., 2023). It demonstrates the optical-derived water occurrence data, taking as an independent observation, provides wave-invariant surface references. Similar, at Pong reservoir in which a stronger windy regime covering 91% of water area (Fig. 8), the proposed method successfully extracted the water area of 232.9 km^2. Semi-permanent inundation zone exhibits decreased cross-polarized (VH) scattering of −7.2 dB from emergent vegetation, while co-polarized (VV) and optical data maintained stable signatures. Fourth, steep terrain (slope > 35°) near Bhakra reservoir induces radar shadows, but multi-feature fusion reduces terrain-related errors. As demonstrated, the dual-polarization SAR and optical-derived water occurrence data enhances hydrological feature extraction through three synergistic mechanisms: 1) VV-polarization demonstrates stability against volume

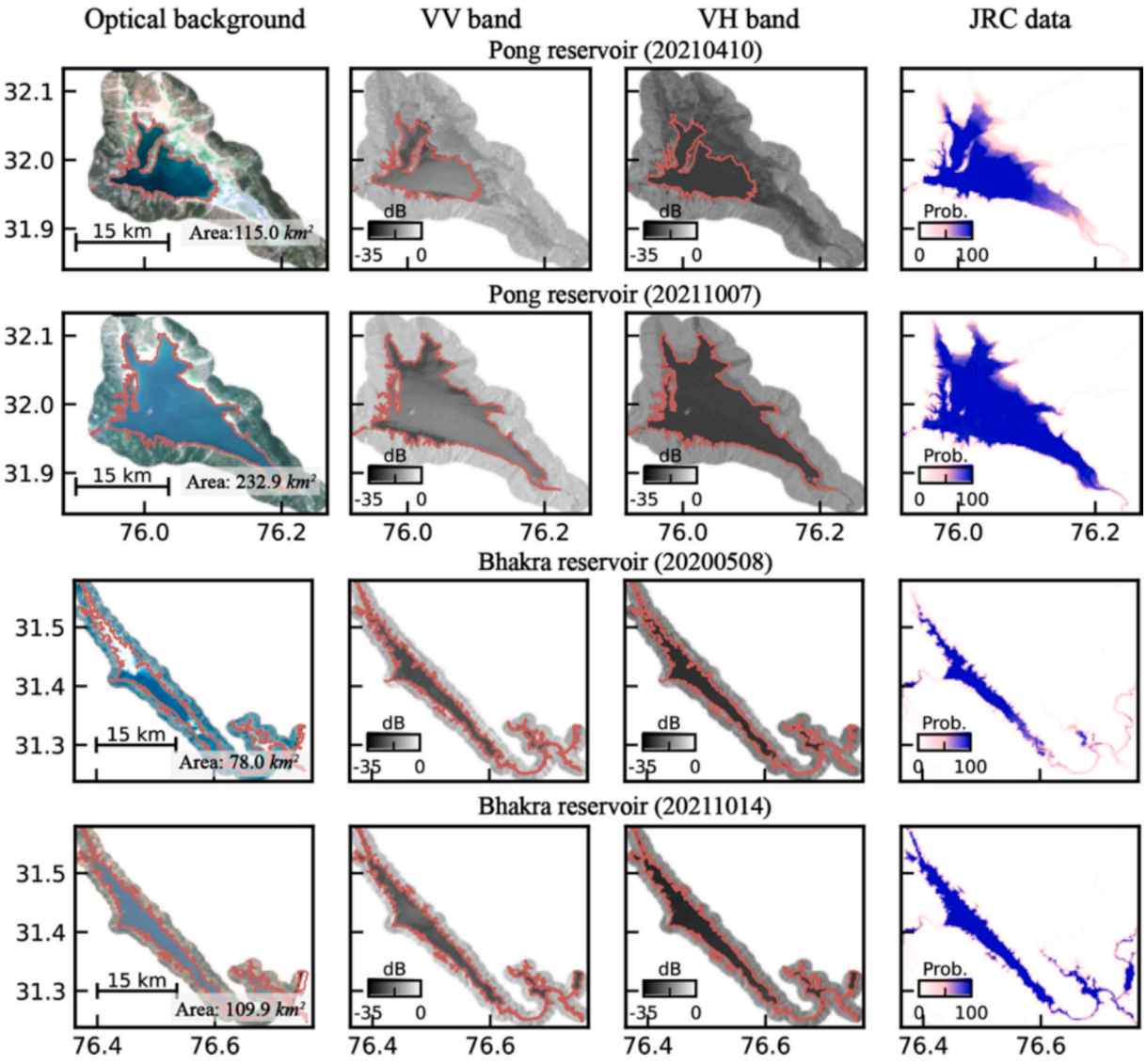

Fig. 8. Similar to Fig. 7 but for Pong reservoir and Bhakra reservoir.

scattering perturbations from soil moisture dynamics and seasonally inundated vegetative interference; 2) VH-polarization effectively suppresses Bragg scattering, and maintains stable aquatic signatures, enabling robust water detection under wind-roughened surfaces; 3) optical-based water occurrence maps provide speckle-free reference surfaces, overcoming coherent noise limitations inherent to single-polarization SAR data. Therefore, the proposed Bayesian probabilistic method optimally weights these complementary features through variational inference with Markov Random Fields regularization, and iteratively minimizing the energy function for multi-source likelihood to solve a continuity water-land boundary.

4.2. Extracted water time series

The estimated water time series indicates that the annual budget of the reservoir water-spread area ranged from 388 km^2 in mid-March to 730 km^2 in mid-September (Fig. 9e). This pattern was consistent with the upstream inflow charged by precipitation and meltwater. However, the annual periodicities of these four reservoirs varied in both amplitude and phase because of the water regulation strategy for irrigation and electricity. The Mangla and Ranjit Sagar reservoirs reached full capacity in August to mid-September. The Pong and Bhakra reservoirs were typically filled between mid-September and early October. The water levels decreased to a minimum in March–April, February–March, June–July, and April–June for Mangla, Ranjit Sagar, Pong, and Bhakra, respectively. In 2019, abnormal water variations may be attributed to the strong and delayed Indian summer monsoon (Xie et al., 2021); the delay of the onset of the monsoon season to July gave rise to abnormal low-water standing in the Mangla (140 km^2), Ranjit Sagar (60 km^2), and Pong (186 km^2) reservoirs (Fig. 9). Successive intense rainfall events in August exerted abrupt impoundments in August and early September (e.g., Fig. 10d) at Mangla Reservoir).

4.3. Validations

We first validated our estimation using two independent measurements, i.e., manual delineation and *in situ* gauges. In the Mangla Reservoir, forty-five manual delineated water boundaries were selected for our quantitative evaluation in Mangla Reservoir. The results were in good agreement, with $R^2 = 0.995$ (Fig. 13a). The RMSE of water area was 4.85 km^2, accounting for 2.5% of the difference in gross areas (Table 1). In addition, the dual-polarization can decrease ~ 2.1% of difference of manual delineation contours comparing with single-polarization inputs, especially for near-shore area as shown in Mangla Reservoir (Fig. 11). Comparing the optical and SAR data, we found that the moister soil near the shoreline, wind-induced Bragg scattering, and mountain shadows could be corrected automatically (Fig. 10). However, the proposed segmentation still exhibits underestimation, when detecting narrow canals or thin stream branches (e.g., Fig. 11, underestimation by dual-band is 3.0 km^2, and VV band is 10.2 km^2). In these cases, the underestimation occurs because the dominant backscatters at the end tips of the stream channels may be the neighboring land, rather

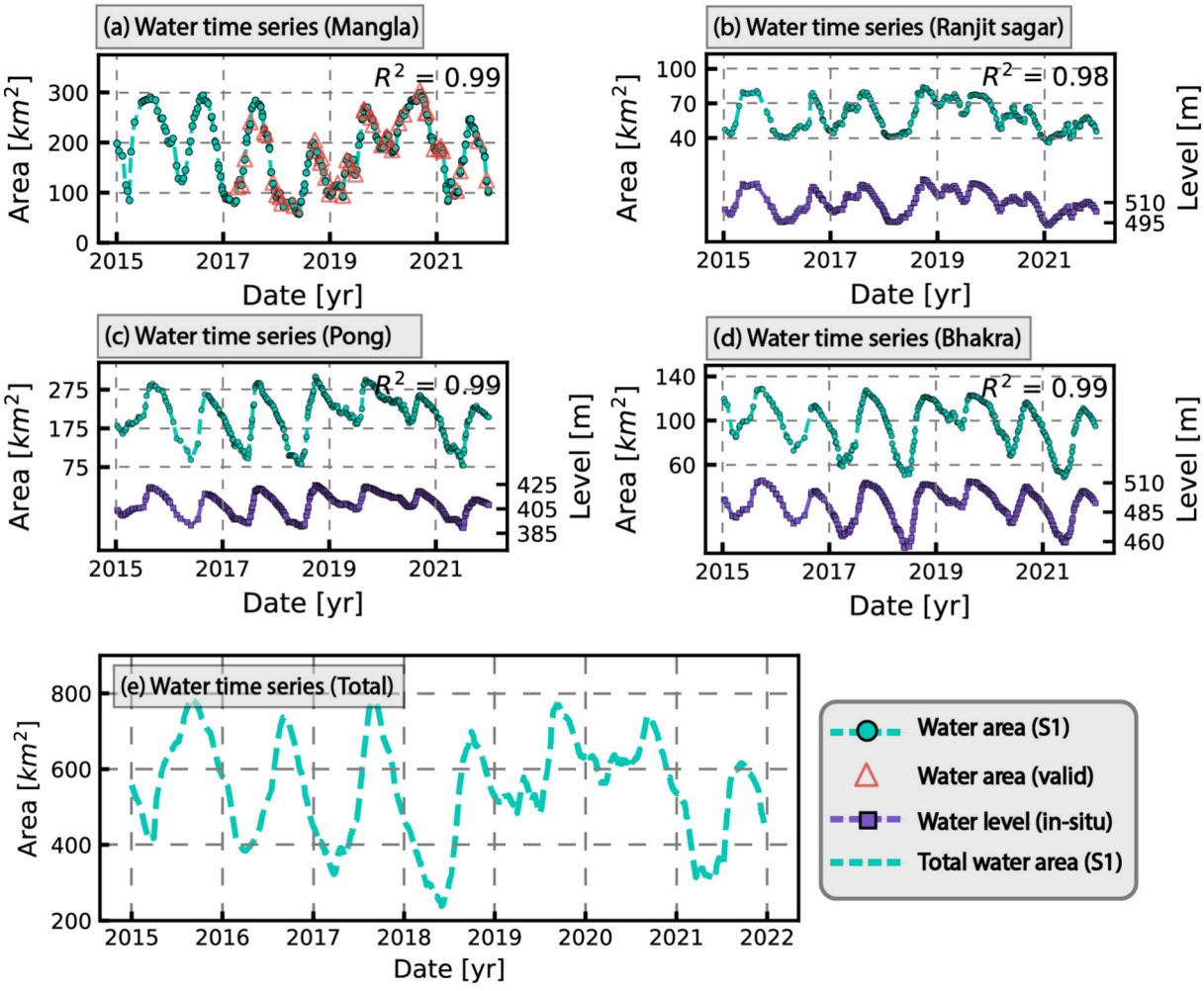

Fig. 9. Water time series and validation. (a) Manual delineated area vs. estimated water area; (b–d) *In situ* water level vs. estimated water area; (e) Total water area variations.

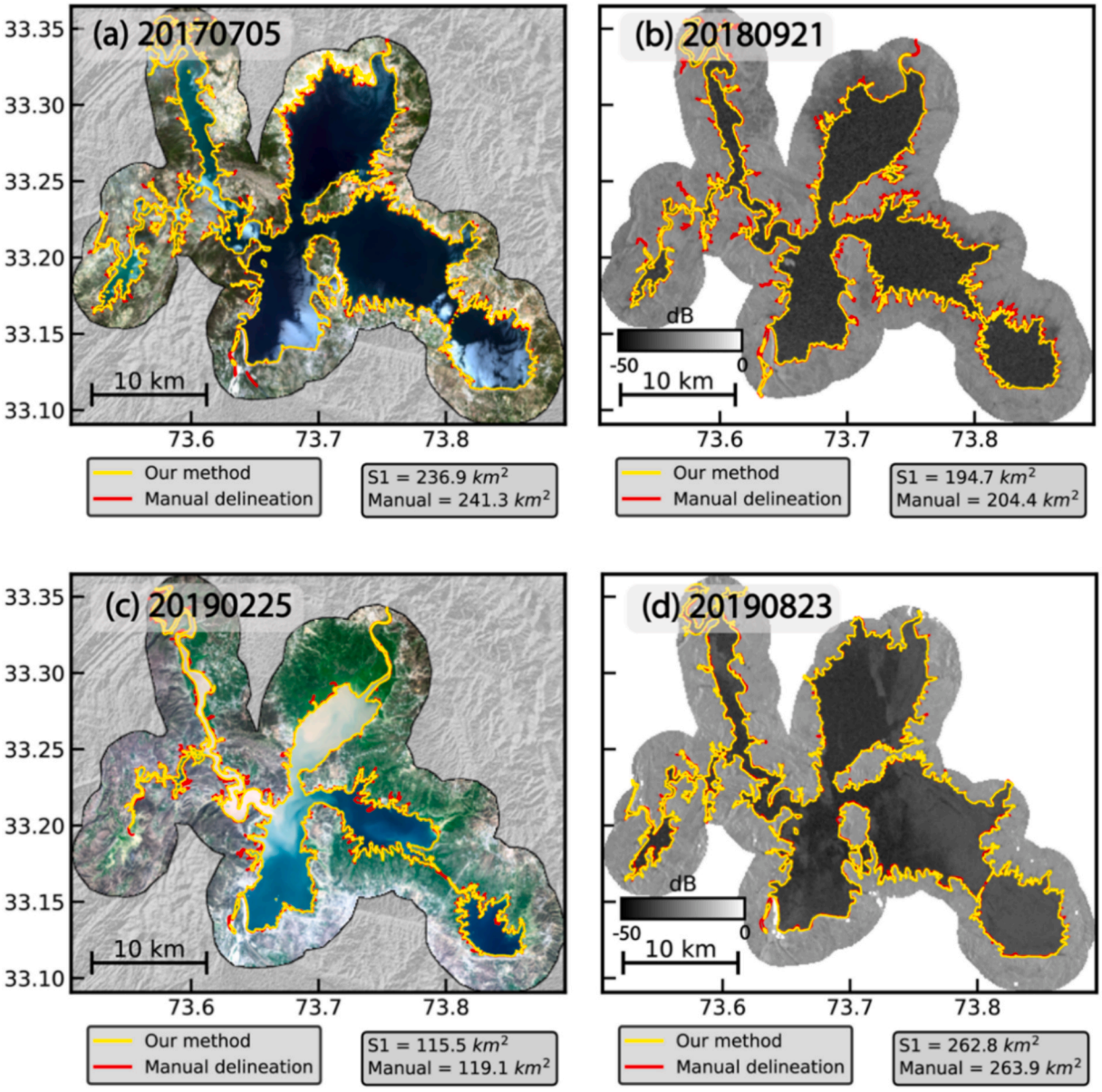

Fig. 10. Comparison between the proposed method and manual delineation. Red: manual delineation from optical data. Yellow: our estimation from S1 data. (Noted that the white pixels within the water extents of the subplot (a) are the reflectance of clouds). (For interpretation of the references to colour in this figure legend, the reader is referred to the web version of this article.)

Table 1
Performance comparison between different methods in Mangla Reservoir.

Methods	RMSE (km^2)	Difference %	Correlation R^2
GMLC	11.92	6.1	0.932
RF + Wishart	11.24	5.8	0.941
Thresholding	24.92	12.8	0.835
Our Method (Single polar)	8.95	4.6	0.962
Our Method (Dual polar)	4.85	2.5	0.995

than the narrow open water (Fig. 11b and c). In addition to underestimation, boundary overestimation may also occur in mixed shoreline pixels, where spatial regularization and prior integration promote boundary continuity (e.g., Fig. 11, overestimation by dual-band is 1.9 km^2, and VV band is 1.4 km^2). Boundary expansion or retreat responds systematically to input ambiguities and reflects an intrinsic trade-off between observation uncertainty and model regularization (see Section 4.4.2).

We further compared our method with other water classification methods in the Mangla reservoir as: 1) statistical-based method using Gaussian Maximum Likelihood Classification (GMLC) model; 2) learning-based method using Random Forest (RF) model with Wishart classifier and manual labels, in which we randomly selected 1000 samples of water and 1000 samples of land to estimate the cluster center; 3) threshold-based method by maximum between-class variance following an additional 5 × 5 median filter. The results show that the proposed method has a better RMSE of 4.85–8.95 km^2 comparing to the existing threshold method (24.92 km^2), RF + Wishart method (11.24 km^2), and GMLC method (11.92 km^2). It achieves less than 5% difference with either single-polarization or dual-polarization. This improvement of precision demonstrates that the proposed method benefits from the contextual enhancement from water occurrence and the Bayesian-based iterative model. In addition, conventional methods exhibited temporal instability ($\geq |3\sigma|$ variation across 10-image sequences, see statistic results in Section 4.4.1). In seasonal agricultural zones (33.31° N, 73.69° E), threshold-based and GMLC outputs has false

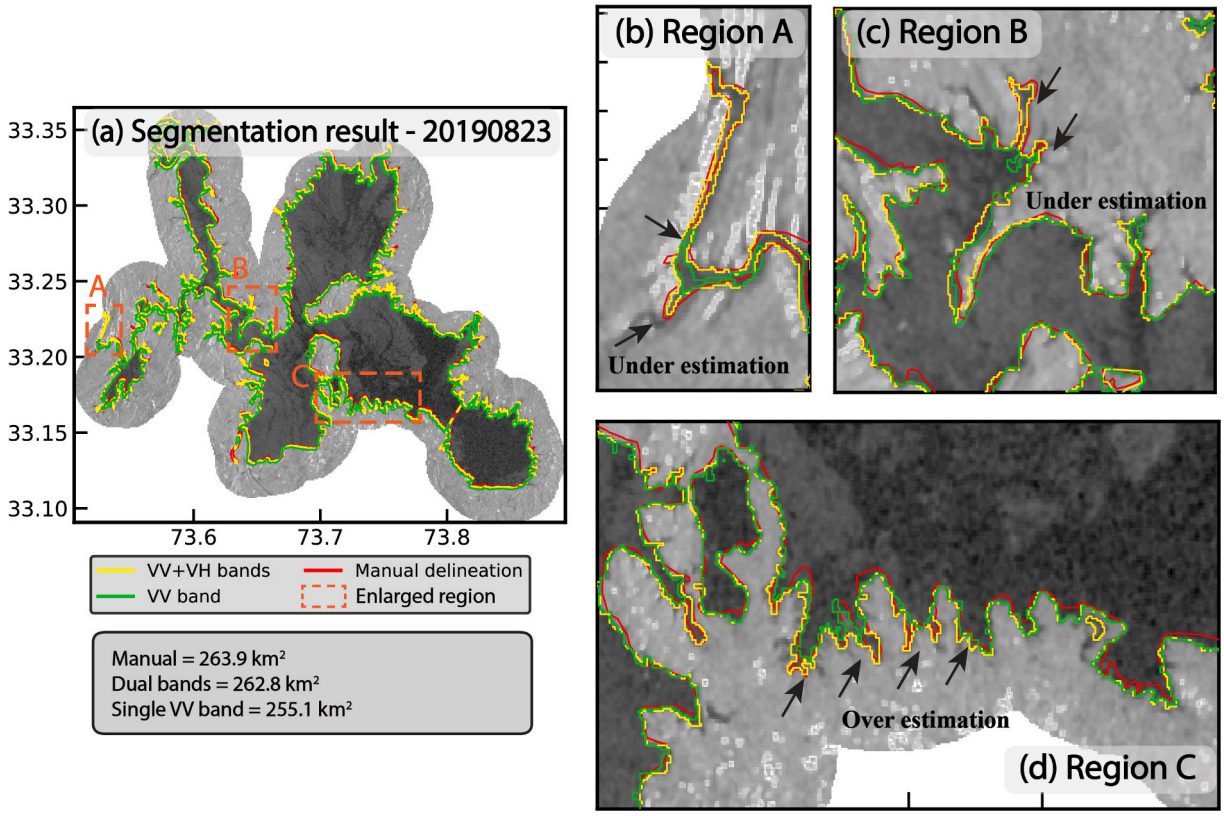

Fig. 11. Comparison of segmentation results between the inputs of polar-band and dual-band in Mangla Reservoir.

positives of 18.8 km^2 and 6.2 km^2, respectively, attributed to ~ 10 dB VH backscatter reduction from elevated soil moisture (Fig. 12b and d). Conversely, Bragg scattering phenomena in open-water regions were misclassified at areas of 70.5 km^2 and 30.4 km^2 using thresholding and RF + Wishart methods, respectively (Fig. 12f and c). Topographic shadows with local slope angle larger than 15 ° induce false water-land transitions in southwest of reservoir (33.23° N, 73.50° E), particularly affecting GMLC outputs (Fig. 12h). Residual speckle noise generated spatially clustered commission errors near the shorelines (Fig. 12g and h), accounting for tens of square kilometers in the lakeshore.

We also used the daily *in situ* gauge from CWC of India, as an independent validation data, at the other three reservoir sites to evaluate the estimation performance. We conducted the correlation analysis between the gauged water level and water areas estimated from proposed method. The correlation coefficients R^2 for Ranjit Sagar, Pong, and Bhakra reservoirs are 0.98, 0.99, and 0.99, respectively (Fig. 13). We also quantified the RMSE by applying local polynomial and linear regressions from 1,000 bootstrap iterations. Similar to the results of manual delineation, the RMSEs between the fitted water area from area-level curve and the estimated water area accounts for the 3.9% of water area in Ranjit Sagar, 4.5% in Pong, and 2.1% in Bhakra.

4.4. Discussion

4.4.1. Enhancement of the weekly monitoring

In this paper, we proposed a new Bayesian-based method that in-

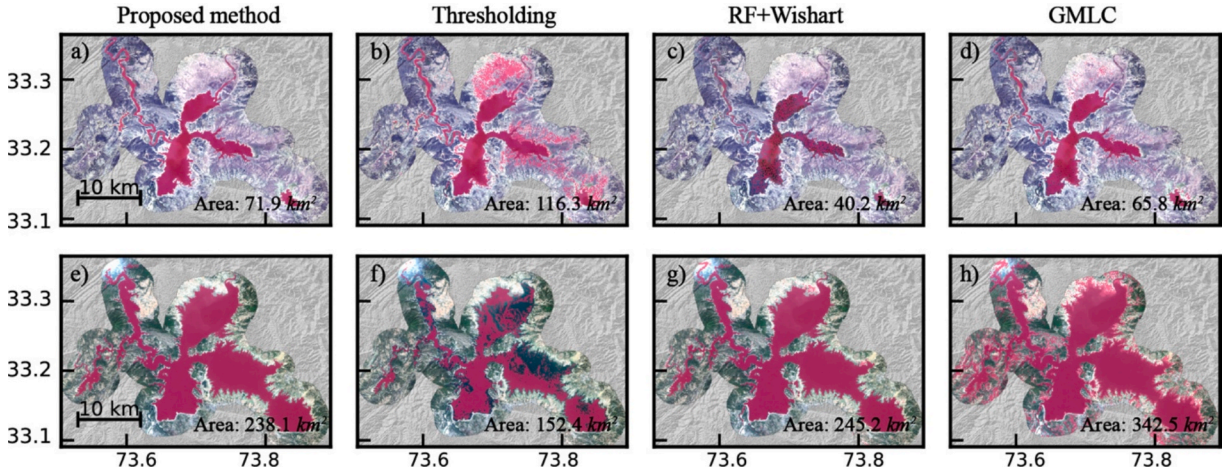

Fig. 12. Comparison of segmentation results between different methods. First row: example of low-water standing period (20200430); second row: example of high-water standing period (20171008). The polarization data can refer to the Fig. 7.

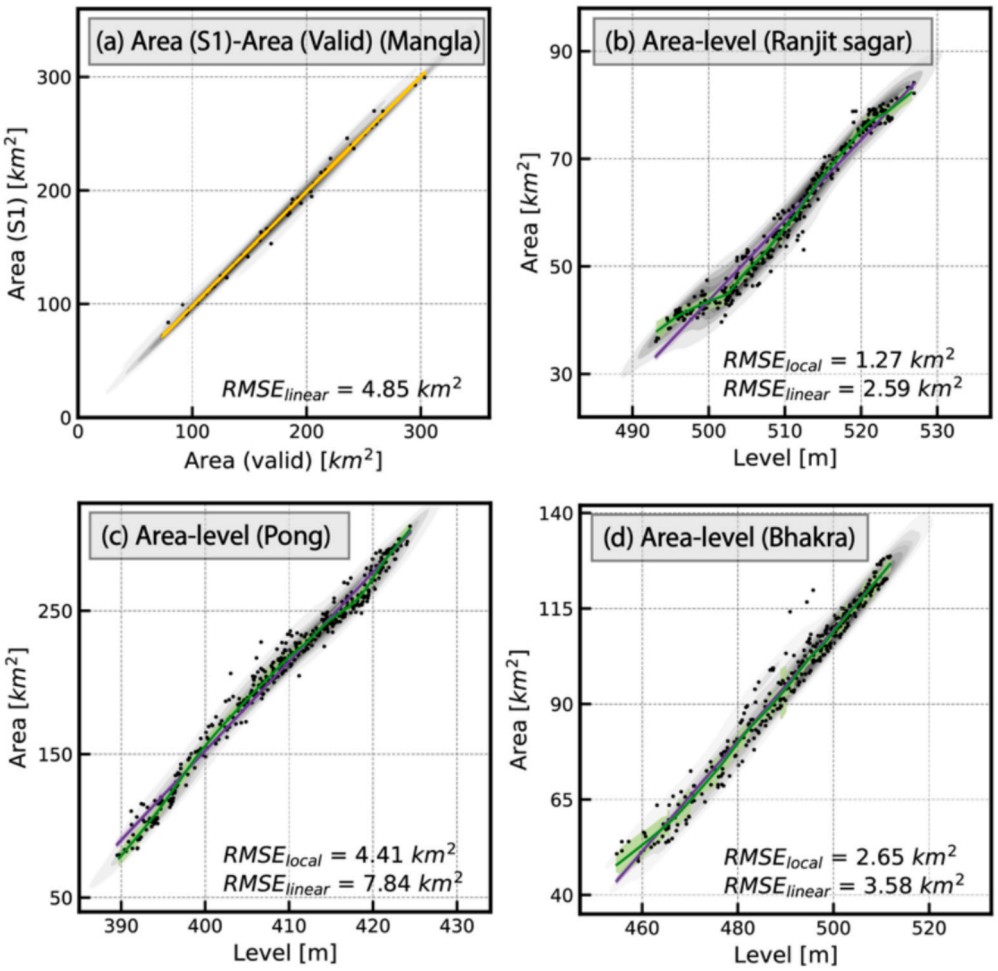

Fig. 13. The correlation of estimated area and validations. (a) The linear correlation between the manual delineation and estimated water area. (b–d) The correlations between water level and estimated water area. The yellow and purple lines indicate linear fittings. The green lines are the regional polynomial fitting. (For interpretation of the references to colour in this figure legend, the reader is referred to the web version of this article.)

corporates the water occurrence and dual-polarization SAR data. As demonstrated in experiments, this method improves segmentation precision against the scattering change due to the wind and soil moisture, and avoid post-processing steps in boundary delineation. Here, we further discuss the effectiveness of proposed method in enhancing the temporal resolution for the reservoir water spread monitoring. We quantify: 1) publicly available datasets with high spatial resolutions (Fig. 14): SAR (S1) vs. optical (Sentinel-2 and Landsat-8); 2) anomalies were identified using the moving temporal window analysis (i.e., water area variations $\geq |3\sigma|$ in the temporal window with a step of 10 acquisitions will be marked as the outliers).

For the Himalayan foothills, the S1 mission provides a revisit period of 6–12 days in most basin areas. Landsat-8 has a temporal resolution of 16 days. Since late 2015, Sentinel-2 has provided a temporal resolution of 5 days or better. However, the average number of cloud-free and partially cloudy images over these four reservoirs was ~ 225 during 2015–2021, equivalent to ~ 11 days per acquisition. Sentinel-1 data provide a denser coverage of ~ 7 days per acquisition. Despite the low temporal resolution of optical images, as expected, the main limitation of optical data is the lack of observations during the rainy season. During the monsoon season, the average number of analysis-ready optical images for July, August, and September were 0.7, 0.8, and 1.9 per month, respectively. Unfortunately, this means that the lowest monitoring frequency corresponds to the period with most rapid reservoir expansion. This challenge can be mitigated, to some extent, by using more optical satellites. However, as the water gain of a reservoir is accompanied by heavy rainfall, clouds are unavoidable above the reservoirs during the wet season (Gao, 2015; Shin et al., 2020). In contrast, radiation from a microwave sensor can penetrate clouds and is effective under all weather conditions. Despite several acquisitions being contaminated by radio frequency interference, almost all acquisitions are analysis ready, bringing routine and effective monitoring, with 4.1, 4.5, and 4.7 images in July, August, and September, respectively.

Second, comparative analysis with conventional methods: 1) Thresholding, 2) RF-Wishart, and 3) GMLC, revealed failure rates of 16.6% (238 cases), 7.6% (109 cases), and 6.1% (87 cases) respectively, across the acquisition dataset (Fig. 14). As detailed in Section 4.3, principal failure mechanisms included dynamic backscattering modulations at water-land interfaces and persistent speckle noise residuals. The proposed method demonstrated a 6.4%-18.0% improvement in effective temporal resolution, achieving 7.3 days compared to conventional approaches: 8.9 days (Thresholding), 7.9 days (RF-Wishart), and 7.8 days (GMLC).

4.4.2. *Sensitivity of the water occurrence data*

To quantify the sensitivity of proposed method towards input water occurrence data, a synthetic water occurrence dataset with systematic probability gradients (10%-90%) was generated from the original JRC data (Fig. 15). Two 3.3 × 3.3 km lakeshore regions were selected for experiments: 1) Transitional zone (Area 1): An agro-aquatic interface exhibiting pronounced seasonal inundation patterns and dynamic soil moisture variations (e.g., Fig. 15e and f, −16 dB to −26 dB from VV to

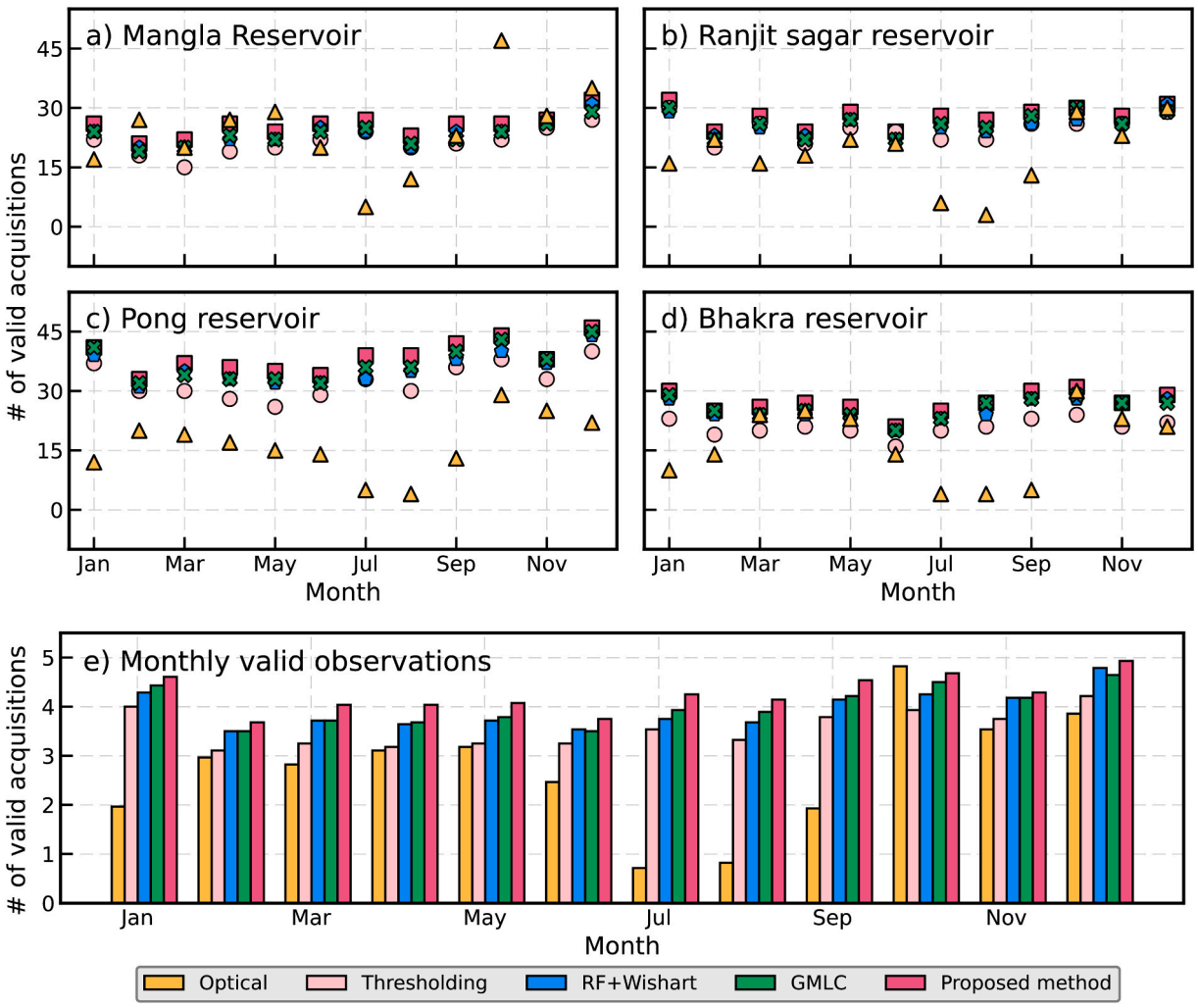

Fig. 14. Statistics of valid observations. (a–d) Successful extraction of water area using different methods during the period 2015–2021. (e) Monthly average for valid observations.

VH band). 2) Open water (Area 2): An area mixed with permanent water body and frequently exposed sediments, which is more likely to encounter the Bragg scattering characteristics (e.g., VV-VH $>$ 5 dB during the high-wind condition). The results revealed $\leq$ 5.5% and $\leq$ 9.7% relative area deviations under 30% probability reduction/increase scenarios respectively, demonstrating method robustness against input inaccuracies of water occurrence (Fig. 15c and d). These discrepancies are mainly raised from the limited separability between agricultural (-26.3 ± 1.2 dB) and aquatic (-28.1 ± 0.8 dB) in VH polarization (Fig. 15f). In other words, as Bayesian segmentation weights polarization signatures against water occurrence probabilities, it can achieve a better performance with inter-class backscatter separability (Fig. 15g), and vice versa. This demonstrates the method's tolerance threshold for water occurrence inaccuracies (20–30%) while maintaining fidelity across validation sites. However, when water occurrence errors exceed 40%, inherent Bayesian weighting limitations emerge as prior probability distributions become statistically dominant (Fig. 15h), necessitating complementary uncertainty quantification measures.

In addition, the synthetic experiments reveal a systematic boundary response to input data and model's MRF-based spatial regularization. Positive perturbations lead to boundary expansion in transitional shoreline zones as mixed shoreline pixel, whereas negative perturbations result in boundary retreat, particularly in regions dominated by narrow tips. This behavior indicates that boundary overestimation and underestimation are not random artifacts, but rather reflect how the Bayesian inference framework balances polarization-based likelihoods against probabilistic priors during iterative MAP optimization.

4.4.3. *Computational efficiency*

For the potential large-scale application, we further tested the computation burden of the proposed method. All algorithms were run on the Intel Xeon (R) W-2255 @ 3.70 GHz with the input image size of 1087 $\times$ 1296 (Table 2). A total 200 images were tested to better evaluate the variations of computational time. The result shows that the thresholding method is fastest with its simple maximize of inter-class histogram procedure for segmentation. The speeds for GMLC and RF + Wishart are comparable, with each segmentation run taking mostly less than 10 s. However, our method has drawbacks 5x-20x slower than other methods because of: 1) the high-dimensional of input data; 2) 100–200 times of iterations including the burn-in and estimation periods. Consequently, it takes 30–80 s for each image depending on the numbers of polarization that has been fed into the model.

4.4.4. *Future perspectives*

First, although the selected medium-to-large reservoirs (~50–150 km^2) already exhibit diverse shoreline geometries, strong hydrological variability, and challenging SAR scattering conditions, systematic extension to small reservoir scales ($<$5 km^2) remains an important next step. In particular, low-albedo surfaces, vegetated water, and pronounced shoreline fragmentation in small open reservoirs call for scale-

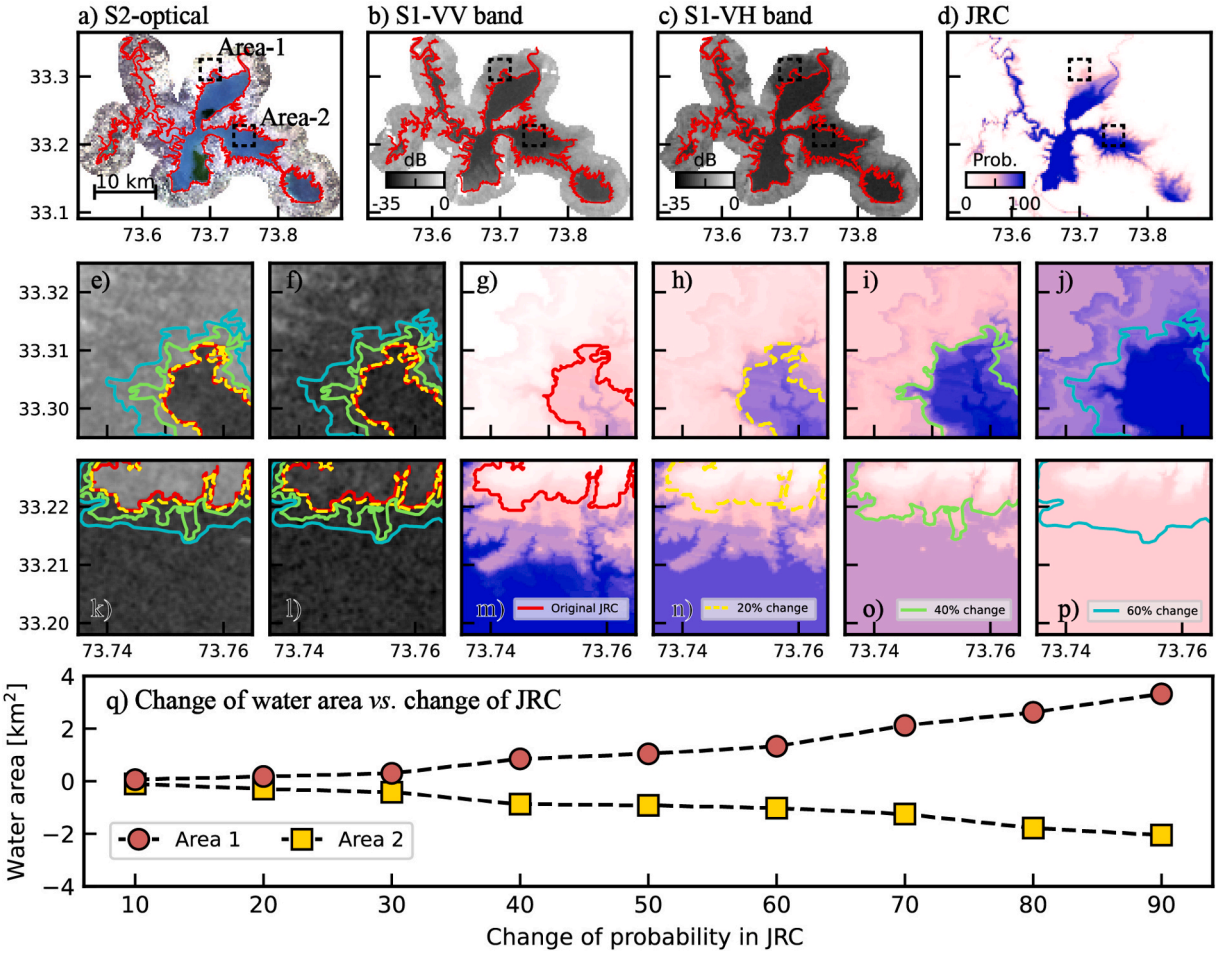

Fig. 15. Result of water area extraction with synthetic JRC data. First row: optical image and input dataset (i.e., Sentinel-1 and JRC data). Two dashed boxes denote the areas for the synthetic JRC data. Second row: Area-1 increases of JRC with 20, 40, 60 in probability. Third row: Area-2 decreases of JRC with 20, 40, 60 in probability. Fourth row: the changes of estimated water area with synthetic JRC data.

Table 2
Computational speed for different methods.

Methods	Image size	Time of single run (s)	Total time (s)
GMLC		6.2–8.5	1,642
RF + Wishart	1087 × 1296 × 1	4.5–6.4	1,102
Thresholding		1.5–2.2	344
Our Method (Single)	1087 × 1296 × 2	37.8–52.2	8,440
Our Method (Dual)	1087 × 1296 × 3	55.1–80.7	12,840

aware adaptations of the proposed framework, including higher-resolution SAR data, enhanced polarimetric or texture-based features, and adaptive spatial regularization strategies (Chen et al., 2024).

Second, this study focuses on ice-free reservoir conditions. Water bodies affected by seasonal ice cover or freeze–thaw processes represent a fundamentally different SAR scattering regime, where frozen surfaces may exhibit stronger and fragmented back-scattering signals. The radiative transfer model (Murfitt et al., 2023) which determines the ice-water interface roughness, and multi-polarization index (Dai et al., 2022) which increases the texture feature of the ice/snow target can be integrated to the current Bayesian framework to improve adaptations.

Third, by improving the spatial resolution and robustness of reservoir boundary delineation to a weekly basis, this study provides a practical pathway to reliably map reservoir in optical-denied environment, such as South Asia and other humid tropical regions. Furthermore, it can combine with reconstructed global bathymetric or hypsometric information (Huang et al., 2025) and gap-free precipitation fields (J. Wang et al., 2025) to support hydrological applications, including water storage assessment, drought and flood monitoring, and model calibration in data-scarce regions.

5. Conclusion

In this study, we propose a Bayesian segmentation method to delineate the water-spread area of reservoirs. Integrating SAR intensity images and water occurrence data improves reservoir water monitoring to one-week temporal resolution. Our experiments show good agreement when compared with manual delineation ($RMSE = 4.85 km^2$ and $R^2 = 0.995$), *in situ* measurements ($RMSE = 1.27 - 7.84 km^2$ and $R^2 = 0.98$), and other three methods ($RMSE = 11.24 - 24.92 km^2$ and $R^2 = 0.84 - 0.94$). The proposed method enhances temporal monitoring capacity by 6–18% and 34% compared to conventional SAR methods and optical method, achieving a 7.3-day effective observation frequency. We found that four large reservoirs in the Himalayan foothills modulate a water expansion of ~ 342 km^2. While these four reservoirs have similar climates and are controlled by the Indian summer monsoon, the exact phases and amplitudes of each reservoir are different. With an increased number of available SAR missions in the near future, the wide and dense coverage of SAR-based water monitoring can shed more lights on reservoir dynamics on a weekly basis, especially in humid areas such as southeast Asia and the Amazon.

CRediT authorship contribution statement

Lei Xie: Writing – review & editing, Writing – original draft, Visualization, Validation, Software, Methodology, Investigation, Funding acquisition, Formal analysis, Data curation, Conceptualization. **Wenbin Xu:** Writing – review & editing, Project administration, Methodology, Investigation, Funding acquisition, Formal analysis. **Kun Jiang:** Writing – review & editing, Investigation. **Lei Zhao:** Writing – review & editing. **Eslam Ali:** Writing – review & editing.

Declaration of competing interest

The authors declare that they have no known competing financial interests or personal relationships that could have appeared to influence the work reported in this paper.

Acknowledgements

The research is supported by the National Natural Science Foundation of China (42304037), Natural Science Foundation of Hunan Province (2025JJ60239, 2024JJ3031), and Hunan Province Dam Safety and Disease Prevention Engineering Research Center (Hndam2023kf05). We thank for the ESA, USGS, Central Water Commission India (https://cwc.gov.in/reservoir-level-storage-bulletin) for the Sentinel-1, Sentinel-2, Landsat-8, and gauge measurement, respectively. We acknowledge the High Performance Computing Center of Central South University for support. Global Reservoir and Dam Database is a product of the Global Water System Project (http://globaldamwatch.org/grand/). Some figures are prepared by the GMT 6.0 (https://www.generic-mapping-tools.org/).

Appendix A. Supplementary data

Supplementary data to this article can be found online at https://doi.org/10.1016/j.jhydrol.2026.135498.

Data availability

Data will be made available on request.

References

Adams, R.D., Ahmed, A., 1969. Seismic effects at Mangla Dam, Pakistan. Nature 222, 1153–1155. https://doi.org/10.1038/2221153a0.

Adeloye, A.J., Soundharajan, B.-S., Ojha, C.S.P., Remesan, R., 2016. Effect of hedging-Integrated rule curves on the performance of the Pong reservoir (India) suring acenario-neutral climate change perturbations. Water Resour. Manag. 30 (2), 445–470. https://doi.org/10.1007/s11269-015-1171-z.

Ahmad, A., El-Shafie, A., Razali, S.F.M., Mohamad, Z.S., 2014. Reservoir optimization in water resources: a review. Water Resour. Manag. 28 (11), 3391–3405. https://doi.org/10.1007/s11269-014-0700-5.

Bookhagen, B., Burbank, D.W., 2010. Toward a complete Himalayan hydrological budget: spatiotemporal distribution of snowmelt and rainfall and their impact on river discharge. J. Geophys. Res. Earth 115 (F3). https://doi.org/10.1029/2009JF001426.

Boulange, J., Naota, H., Dai, Y., Yadu, P., 2021. Role of dams in reducing global flood exposure under climate change. Nat. Commun. 12, 417. https://doi.org/10.1038/s41467-020-20704-0.

Chen, J., Lin, C., Xue, K., Cao, Z., Ma, R., Ma, D., Tong, Y., 2024. Mapping China aquaculture ponds: integrating a new aquaculture index with machine learning. SSRN. https://doi.org/10.2139/ssrn.5011701.

D'Addabbo, A., Refice, A., Pasquariello, G., Lovergine, F.P., Capolongo, D., Manfreda, S., 2016. A Bayesian network for flood detection combining SAR imagery and ancillary data. IEEE Trans. Geosci. Remote Sens. 54 (6), 3612–3625. https://doi.org/10.1109/TGRS.2016.2520487.

Dai, K., Wen, N., Fan, X., Deng, J., Zhang, L., Liang, R., Liu, J., Xu, Q., 2021. Seasonal changes of glacier lakes in Tibetan Plateau revealed by multi-polarization SAR data. IEEE Geosci. Remote Sens. Lett. 1–1. https://doi.org/10.1109/LGRS.2021.3131717.

Dai, K., Wen, N., Fan, X., Deng, J., Zhang, L., Liang, R., Liu, J., Xu, Q., 2022. Seasonal changes of Glacier Lakes in Tibetan Plateau revealed by multipolarization SAR data. IEEE Geosci. Remote Sens. Lett. 19, 1–5. https://doi.org/10.1109/LGRS.2021.3131717.

Dau, Q.V., Adeloye, A.J., 2021. Influence of reservoir joint operation on performance of the Pong–Bhakra multipurpose, multireservoir system in Northern India. J. Water Resour. Plan. Manag. 147 (11), 04021076. https://doi.org/10.1061/(ASCE)WR.1943-5452.0001462.

Donchyts, G., Winsemius, H., Baart, F., Dahm, R., Schellekens, J., Gorelick, N., Iceland, C., Schmeier, S., 2022. High-resolution surface water dynamics in Earth's small and medium-sized reservoirs. Sci. Rep. 12 (1), 1. https://doi.org/10.1038/s41598-022-17074-6.

Dong, N., Wei, J., Yang, M., Yan, D., Yang, C., Gao, H., Arnault, J., Laux, P., Zhang, X., Liu, Y., Niu, J., Wang, H., Wang, H., Kunstmann, H., Yu, Z., 2022. Model estimates of China's terrestrial water storage variation due to reservoir operation. Water Resour. Res. 58 (6). https://doi.org/10.1029/2021WR031787.

Dong, Z., Liang, Z., Wang, G., Amankwah, S.O.Y., Feng, D., Wei, X., Duan, Z., 2023. Mapping inundation extents in Poyang Lake area using Sentinel-1 data and transformer-based change detection method. J. Hydrol. 620, 129455. https://doi.org/10.1016/j.jhydrol.2023.129455.

Ferrentino, E., Nunziata, F., Buono, A., Urciuoli, A., Migliaccio, M., 2020. Multi-polarization time-series of Sentinel-1 SAR imagery to analyze variations of reservoirs' water-body. IEEE J. Sel. Top. Appl. Earth Obs. Remote Sens. 1–1. https://doi.org/10.1109/JSTARS.2019.2961563.

Fjortoft, R., Delignon, Y., Pieczynski, W., Sigelle, M., Tupin, F., 2003. Unsupervised classification of radar images using hidden Markov chains and hidden Markov random fields. IEEE Trans. Geosci. Remote Sens. 41 (3), 675–686. https://doi.org/10.1109/TGRS.2003.809940.

Gao, H., 2015. Satellite remote sensing of large lakes and reservoirs: from elevation and area to storage. WIREs Water 2 (2), 147–157. https://doi.org/10.1002/wat2.1065.

Geman, S., Geman, D., 1984. Stochastic relaxation, gibbs distributions, and the bayesian restoration of images. IEEE Transactions on Pattern Analysis and Machine Intelligence, PAMI-6(6), 721–741. IEEE Transactions on Pattern Analysis and Machine Intelligence. https://doi.org/10.1109/TPAMI.1984.4767596.

Goumehei, E., Tolpekin, V., Stein, A., Yan, W., 2019. Surface water body detection in polarimetric SAR data using contextual complex wishart classification. Water Resour. Res. 55 (8), 7047–7059. https://doi.org/10.1029/2019WR025192.

Gupta, H.K., Rajendran, K., 1986. Large artificial water reservoirs in the vicinity of the Himalayan foothills and reservoir-induced seismicity. Bull. Seismol. Soc. Am. 76 (1), 205–215.

Hjorth, P., Bengtsson, L., 2012. Large dams, statistics and critical review. In: Bengtsson, L., Herschy, R.W., Fairbridge, R.W. (Eds.), Encyclopedia of Lakes and Reservoirs. Springer, Netherlands, pp. 475–479. https://doi.org/10.1007/978-1-4020-4410-6.

Huang, C.H., Zhang, S., Shah, D., Yadav, A., Li, Y., Zhao, G., Gao, H., 2025. 3D-LAKES: three-dimensional global lake and reservoir bathymetry from ICESat-2 altimetry and landsat imagery. Sci. Data 12 (1), 1625. https://doi.org/10.1038/s41597-025-05911-y.

Inserra, G., Buono, A., Nunziata, F., Virelli, M., Migliaccio, M., 2023. On the extraction of the reservoirs' waterline using polarimetric X-band SAR measurements: the case study of the San Giuliano reservoir Italy. Int. J. Remote Sens. 44 (19), 6060–6088. https://doi.org/10.1080/01431161.2023.2261152.

Klein, I., Gessner, U., Dietz, A.J., Kuenzer, C., 2017. Global WaterPack – a 250 m resolution dataset revealing the daily dynamics of global inland water bodies. Remote Sens. Environ. 198, 345–362. https://doi.org/10.1016/j.rse.2017.06.045.

Klein, I., Mayr, S., Gessner, U., Hirner, A., Kuenzer, C., 2021. Water and hydropower reservoirs: high temporal resolution time series derived from MODIS data to characterize seasonality and variability. Remote Sens. Environ. 253, 112207. https://doi.org/10.1016/j.rse.2020.112207.

Lee, J.-S., Wen, J.-H., Ainsworth, T.L., Chen, K.-S., 2009. Improved sigma filter for speckle filtering of SAR imagery. IEEE Trans. Geosci. Remote Sens. 47 (1), 202–213. https://doi.org/10.1109/TGRS.2008.2002881.

Lehner, B., Liermann, C.R., Revenga, C., Vörösmarty, C., Fekete, B., Crouzet, P., Döll, P., Endejan, M., Frenken, K., Magome, J., Nilsson, C., Robertson, J.C., Rödel, R., Sindorf, N., Wisser, D., 2011. High-resolution mapping of the world's reservoirs and dams for sustainable river-flow management. Front. Ecol. Environ. 9 (9), 494–502. https://doi.org/10.1890/100125.

Li, X., Du, Z., Huang, Y., Tan, Z., 2021. A deep translation (GAN) based change detection network for optical and SAR remote sensing images. ISPRS J. Photogramm. Remote Sens. 179, 14–34. https://doi.org/10.1016/j.isprsjprs.2021.07.007.

Liang, J., Liu, D., 2020. A local thresholding approach to flood water delineation using Sentinel-1 SAR imagery. ISPRS J. Photogramm. Remote Sens. 159, 53–62. https://doi.org/10.1016/j.isprsjprs.2019.10.017.

Mukhopadhyay, B., Khan, A., 2014. A quantitative assessment of the genetic sources of the hydrologic flow regimes in Upper Indus Basin and its significance in a changing climate. J. Hydrol. 509, 549–572. https://doi.org/10.1016/j.jhydrol.2013.11.059.

Murfitt, J., Duguay, C., Picard, G., Gunn, G., 2023. Forward modelling of synthetic aperture radar backscatter from lake ice over Canadian Subarctic Lakes. Remote Sens. Environ. 286, 113424. https://doi.org/10.1016/j.rse.2022.113424.

Panahi, M., Rahmati, O., Kalantari, Z., Darabi, H., Rezaie, F., Moghaddam, D.D., Ferreira, C.S.S., Foody, G., Aliramaee, R., Bateni, S.M., Lee, C.-W., Lee, S., 2022. Large-scale dynamic flood monitoring in an arid-zone floodplain using SAR data and hybrid machine-learning models. J. Hydrol. 611, 128001. https://doi.org/10.1016/j.jhydrol.2022.128001.

Pekel, J.-F., Cottam, A., Gorelick, N., Belward, A.S., 2016. High-resolution mapping of global surface water and its long-term changes. Nature 540 (7633), 418–422. https://doi.org/10.1038/nature20584.

Perin, V., Tulbure, M.G., Gaines, M.D., Reba, M.L., Yaeger, M.A., 2021. A multi-sensor satellite imagery approach to monitor on-farm reservoirs. Remote Sens. Environ. 112796. https://doi.org/10.1016/j.rse.2021.112796.

Revilla-Romero, B., Wanders, N., Burek, P., Salamon, P., De Roo, A., 2016. Integrating remotely sensed surface water extent into continental scale hydrology. J. Hydrol. 543, 659–670. https://doi.org/10.1016/j.jhydrol.2016.10.041.

Saha, S., Bovolo, F., Bruzzone, L., 2021. Building change detection in VHR SAR images via unsupervised deep transcoding. IEEE Trans. Geosci. Remote Sens. 59 (3), 1917–1929. https://doi.org/10.1109/TGRS.2020.3000296.

Schlaffer, S., Chini, M., Giustarini, L., Matgen, P., 2017. Probabilistic mapping of flood-induced backscatter changes in SAR time series. Int. J. Appl. Earth Obs. Geoinf. 56, 77–87. https://doi.org/10.1016/j.jag.2016.12.003.

Shang, R., Liu, M., Lin, J., Feng, J., Li, Y., Stolkin, R., Jiao, L., 2022. SAR image segmentation based on constrained smoothing and hierarchical label correction. IEEE Trans. Geosci. Remote Sens. 60, 1–16. https://doi.org/10.1109/TGRS.2021.3076446.

Shen, W., Zhang, X., 2016. The effect of large reservoirs impoundment to the spatial and temporal variations of regional crustal deformation in Hubei Province China. Geodesy Geodyn. 7 (5), 377–386. https://doi.org/10.1016/j.geog.2016.06.002.

Shin, S., Pokhrel, Y., Yamazaki, D., Huang, X., Torbick, N., Qi, J., Pattanakiat, S., Ngo-Duc, T., Nguyen, T.D., 2020. High resolution modeling of river-floodplain-reservoir inundation dynamics in the Mekong River Basin. Water Resour. Res. 56 (5). https://doi.org/10.1029/2019WR026449.

Tan, J., Tang, Y., Liu, B., Zhao, G., Mu, Y., Sun, M., Wang, B., 2023. A self-adaptive thresholding approach for automatic water extraction using Sentinel-1 SAR imagery based on OTSU algorithm and distance block. Remote Sens. (Basel) 15 (10), 2690. https://doi.org/10.3390/rs15102690.

Thakur, P.K., Garg, V., Kalura, P., Agrawal, B., Sharma, V., Mohapatra, M., Kalia, M., Aggarwal, S.P., Calmant, S., Ghosh, S., Dhote, P.R., Sharma, R., Chauhan, P., 2021. Water level status of Indian reservoirs: a synoptic view from altimeter observations. Adv. Space Res. 68 (2), 619–640. https://doi.org/10.1016/j.asr.2020.06.015.

Valman, S.J., Boyd, D.S., Carbonneau, P.E., Johnson, M.F., Dugdale, S.J., 2024. An AI approach to operationalise global daily PlanetScope satellite imagery for river water masking. Remote Sens. Environ. 301, 113932. https://doi.org/10.1016/j.rse.2023.113932.

Vanthof, V., Kelly, R., 2019. Water storage estimation in ungauged small reservoirs with the TanDEM-X DEM and multi-source satellite observations. Remote Sens. Environ. 235, 111437. https://doi.org/10.1016/j.rse.2019.111437.

Wang, J., Chen, J., Shen, P., Guan, X., Liu, X., Massari, C., Wang, Z., Feng, M., Wang, Q., Lu, Y., Wei, E., Wang, Y., Umirzakov, G., Yong, B., 2025. Regional-scale intelligent optimization and topography impact in restoring global precipitation data gaps. Commun. Earth Environ. 6 (1), 671. https://doi.org/10.1038/s43247-025-02624-3.

Wang, L., Qu, J.J., 2007. NMDI: a normalized multi-band drought index for monitoring soil and vegetation moisture with satellite remote sensing. Geophys. Res. Lett. 34 (20), 2007GL031021. https://doi.org/10.1029/2007GL031021.

Wheeler, K.G., Jeuland, M., Hall, J.W., Zagona, E., Whittington, D., 2020. Understanding and managing new risks on the Nile with the Grand Ethiopian Renaissance Dam. Nat. Commun. 11 (1), 5222. https://doi.org/10.1038/s41467-020-19089-x.

Xie, L., Xu, W., Bürgmann, R., Ding, X., Gahalaut, V.K., Mondal, S., 2021a. Tehri Reservoir operation modulates seasonal elastic crustal deformation in the Himalaya. J. Geophys. Res. Solid Earth 126 (8), 2020JB021122. https://doi.org/10.1029/2020JB021122.

Xie, L., Xu, W., Ding, X., 2022. Precursory motion and deformation mechanism of the 2018 Xe Pian-Xe Namnoy dam Collapse, Laos: Insights from satellite radar interferometry. Int. J. Appl. Earth Obs. Geoinf. 109, 102797. https://doi.org/10.1016/j.jag.2022.102797.

Xie, L., Xu, W., Liu, X., Ding, X., 2021b. Surge of Mangla reservoir loading promoted failure on active Décollement of western Himalayas. Int. J. Appl. Earth Obs. Geoinf. 102, 102401. https://doi.org/10.1016/j.jag.2021.102401.

Yamazaki, D., Trigg, M.A., Ikeshima, D., 2015. Development of a global ~90m water body map using multi-temporal Landsat images. Remote Sens. Environ. 171, 337–351. https://doi.org/10.1016/j.rse.2015.10.014.

Yang, X., Qin, Q., Yésou, H., Ledauphin, T., Koehl, M., Grussenmeyer, P., Zhu, Z., 2020. Monthly estimation of the surface water extent in France at a 10-m resolution using Sentinel-2 data. Remote Sens. Environ. 244, 111803. https://doi.org/10.1016/j.rse.2020.111803.

Yu, Z., An, Q., Liu, W., Wang, Y., 2022. Analysis and evaluation of surface water changes in the lower reaches of the Yangtze River using Sentinel-1 imagery. J. Hydrol.: Reg. Stud. 41, 101074. https://doi.org/10.1016/j.ejrh.2022.101074.

Zhang, G., Yao, T., Shum, C.K., Yi, S., Yang, K., Xie, H., Feng, W., Bolch, T., Wang, L., Behrangi, A., Zhang, H., Wang, W., Xiang, Y., Yu, J., 2017a. Lake volume and groundwater storage variations in Tibetan Plateau's endorheic basin. Geophys. Res. Lett. 44 (11), 5550–5560. https://doi.org/10.1002/2017GL073773.

Zhang, H., Gorelick, S.M., Zimba, P.V., Zhang, X., 2017b. A remote sensing method for estimating regional reservoir area and evaporative loss. J. Hydrol. 555, 213–227. https://doi.org/10.1016/j.jhydrol.2017.10.007.

Zhang, J., Xing, M., Sun, G.-C., Chen, J., Li, M., Hu, Y., Bao, Z., 2021. Water body detection in high-resolution SAR images with cascaded fully-convolutional network and variable focal loss. IEEE Trans. Geosci. Remote Sens. 59 (1), 316–332. https://doi.org/10.1109/TGRS.2020.2999405.

Zhang, Y., Brady, M., Smith, S., 2001. Segmentation of brain MR images through a hidden Markov random field model and the expectation-maximization algorithm. IEEE Trans. Med. Imaging 20 (1), 45–57. https://doi.org/10.1109/42.906424.

Zhao, G., Li, Y., Zhou, L., Gao, H., 2022. Evaporative water loss of 1.42 million global lakes. Nat. Commun. 13 (1), 3686. https://doi.org/10.1038/s41467-022-31125-6.

Zhou, X., Zhang, Z., Chen, Q., Liu, X., 2020. A practical plateau lake extraction algorithm combining novel statistical features and Kullback–Leibler distance using synthetic aperture radar imagery. IEEE J. Sel. Top. Appl. Earth Obs. Remote Sens. 13, 4702–4713. https://doi.org/10.1109/JSTARS.2020.3016349.